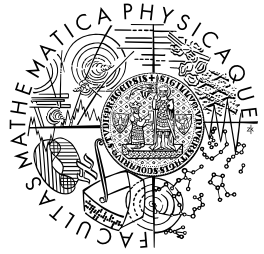


1 nterthm0

2

setcounterdefn0



FACULTY
OF MATHEMATICS
AND PHYSICS
Charles University

3

BACHELOR THESIS

4

Martin Vavřík

5

**Simulation and Reconstruction
of Charged Particle Trajectories
in an Atypic Time Projection Chamber**

6

7

Institute of Particle and Nuclear Physics

8

Supervisor of the bachelor thesis: Mgr. Tomáš Sýkora, Ph.D.

9

Study programme: Physics

10

Prague 2025

- ¹¹ I declare that I carried out this bachelor thesis independently, and only with the
¹² cited sources, literature and other professional sources. It has not been used to
¹³ obtain another or the same degree.
- ¹⁴ I understand that my work relates to the rights and obligations under the Act
¹⁵ No. 121/2000 Sb., the Copyright Act, as amended, in particular the fact that the
¹⁶ Charles University has the right to conclude a license agreement on the use of this
¹⁷ work as a school work pursuant to Section 60 subsection 1 of the Copyright Act.

In date
Author's signature

¹⁸ Dedication.

Title: Simulation and Reconstruction of Charged Particle Trajectories in an Atypical Time Projection Chamber **Added hyphen to avoid overfull hbox**

Author: Martin Vavřík

Institute: Institute of Particle and Nuclear Physics

Supervisor: Mgr. Tomáš Sýkora, Ph.D., Institute of Particle and Nuclear Physics

Abstract: Abstract.

Keywords: key words

¹⁹ Contents

20	Motivation	2
21	0.1 ATOMKI Anomaly	2
22	0.1.1 ATOMKI Measurements	2
23	0.1.2 Other Experiments	3
24	0.2 X17 Project at IEAP CTU	5
25	1 Time Projection Chamber	8
26	1.1 Charge transport in gases	8
27	1.1.1 Drift	8
28	1.1.2 Diffusion	9
29	1.2 Readout	10
30	1.2.1 Multi-Wire Proportional Chamber	10
31	1.2.2 Gas Electron Multiplier	10
32	1.2.3 Micromegas	11
33	1.2.4 Parallel Plate Chamber	11
34	1.3 Orthogonal Fields TPC at IEAP CTU	11
35	1.3.1 Motivation and Associated Challenges	11
36	1.3.2 Coordinate Systems and Dimensions	12
37	1.3.3 Magnetic Field Simulation	14
38	2 Track Simulation	17
39	2.1 Microscopic Simulation	17
40	2.2 Runge-Kutta Simulation	18
41	3 Track Reconstruction	19
42	3.1 Reconstruction Assuming Steady Drift	19
43	3.2 Ionization Electron Map	21
44	3.2.1 Gradient Descent Search	24
45	3.2.2 Interpolation on the Inverse Grid	25
46	3.3 Discrete Reconstruction	26
47	4 Energy Reconstruction	28
48	4.1 Cubic Spline Fit	28
49	4.2 Circle and Lines Fit	30
50	4.2.1 Two-dimensional fit	30
51	4.2.2 Three-dimensional fit	32
52	4.3 Runge-Kutta Fit	34
53	Conclusion	36
54	Bibliography	39
55	List of Figures	43
56	List of Tables	45

58 Motivation

59 A Time Projection Chamber (TPC) [refs] is a type of gaseous detector that detects
60 charged particle trajectories by measuring the positions and drift time of ions cre-
61 ated in the gas. The energies of these particles can be inferred from the curvatures
62 of their trajectories in the magnetic field (specific field inside the TPC).

63 The goal of this thesis is to develop an algorithm for the reconstruction of
64 charged particle trajectories and energy in an *atypic* TPC with orthogonal elec-
65 tric and magnetic fields, hereafter referred to as the Orthogonal Fields TPC
66 (OFTPC), used in the X17 project at the Institute of Experimental and Applied
67 Physics, Czech Technical University in Prague (IEAP CTU). Furthermore, we
68 present the results of testing of several (gradually improving) developed algo-
69 rithms with different samples of simulated data. Put this somewhere, (maybe
70 just the abstract?). We use the Garfield++ toolkit [1] for simulations in combina-
71 tion with the ROOT framework [2] for data analysis and visualization. Some of
72 our more demanding simulations are run on the MetaCentrum grid [3].

73 The X17 project in IEAP CTU aims to reproduce measurements of anomalous
74 behavior in the angular correlation distribution of pairs produced by the Internal
75 Pair Creation (IPC) mechanism [4] during the decay of certain excited nuclei
76 (${}^8\text{Be}$, ${}^{12}\text{C}$, and ${}^4\text{He}$) observed by a team at ATOMKI in Hungary. I would leave
77 this here as a short summary before I explain it in more detail in the sections
78 below.

79 Add citations: X17 project, VdG. Maybe also TPC, etc.

80 0.1 ATOMKI Anomaly

81 Many different theories propose the existence of *new light bosons* that are weakly
82 coupled to ordinary matter [5]. These particles are potential dark matter candi-
83 dates and could solve other issues with the Standard Model, such as the strong
84 CP problem and the anomalous muon magnetic moment.

85 A possible way of detecting such bosons with a short lifetime is to observe
86 nuclear transitions of excited nuclei. If a boson was emitted during the transition
87 and subsequently decayed into an electron-positron pair, we could observe this
88 as a peak on top of the standard e^+e^- angular correlation from the Internal Pair
89 Creation (IPC) and the External Pair Creation (EPC).

90 0.1.1 ATOMKI Measurements

91 Historically, there were several measurements of the IPC in nuclear transitions
92 in ${}^8\text{Be}$ at Institute für Kernphysik (Frankfurt) [6, 7, 8] and at ATOMKI [9, 10]
93 resulting in different anomalies with invariant mass in the range 5–15 MeV. This
94 prompted a development of a better spectrometer at ATOMKI.

95 In 2015, a group at ATOMKI led by Attila Krasznahorkay observed an anom-
96 arious IPC in ${}^8\text{Be}$ [11]. They used the ${}^7\text{Li}(p, \gamma){}^8\text{Be}$ reaction at the $E_p = 1030$ keV
97 proton capture resonance to prepare the 18.15 MeV excited state ($J^\pi = 1^+, T =$
98 = 0). This state decays predominantly through M1 transitions to the ground
99 state ($J^\pi = 0^+, T = 0$) and to the 3.03 MeV state ($J^\pi = 2^+, T = 0$) [12].

100 The angular correlation of the e^+e^- pairs created internally in these transitions
101 were measured and compared to the simulation; results from a narrow $E_{\text{sum}} =$
102 = 18 MeV region are shown in Figure 0.1a. The simulation includes boson decay
103 pairs for different boson masses. The disparity parameter y is defined as

$$y = \frac{E_{e^-} - E_{e^+}}{E_{e^-} + E_{e^+}}, \quad (0.1)$$

104 where E_{e^-} and E_{e^+} are the kinetic energies of the electron and positron.

105 Their experimental setup was later upgraded ([details?](#)) and used for new mea-
106 surements. In 2022 the ${}^8\text{Be}$ anomaly was also measured using the $E_p = 441$ keV
107 resonance to produce the 17.64 MeV excited state ($J^\pi = 1^+$, $T = 1$) which again
108 decays primarily to the ground state and the 3.03 MeV state [12]. The anomaly
109 was also measured for $E_p = 650$ and 800 keV where E1 transitions from the direct
110 proton capture dominate [13]. The results for e^+e^- with $E_{\text{sum}} \in [13.5, 20]$ MeV
111 are shown in Figure 0.1b.

112 The newer setup was also used in 2021 to study the ${}^3\text{H}(p, e^+e^-){}^4\text{He}$ reaction at
113 $E_p = 510, 610$ and 900 keV [14], inducing direct and resonant capture populating
114 the overlapping first 20.21 MeV ($J^\pi = 0^+$) and second 21.01 MeV ($J^\pi = 0^-$)
115 excited states [15]. The comparison of simulated and measured e^+e^- pair angular
116 correlations in the $E_{\text{sum}} \in [18, 22]$ MeV region is shown in Figure 0.1c.

117 In 2022, another anomaly was measured in the ${}^{11}\text{B}(p, e^+e^-){}^{12}\text{C}$ process [16].
118 The $E_p = 1388$ keV resonance was used to populate the 17.23 MeV excited state
119 ($J^\pi = 1^-, T = 1$) with a large width $\Gamma = 1.15$ MeV [17]. This state decays
120 mainly through E1 transitions to the ground state $J^\pi = 0^+$ and to the 4.44 MeV
121 state $J^\pi = 2^+$. To compensate for energy losses in the target, five energies in
122 the range $E_p = 1.5\text{--}2.5$ MeV were used. The experimental angular correlation for
123 the 17.23 MeV transition to the ground state is shown in Figure 0.1d.

124 Possible explanations of the anomaly include experimental effects, higher or-
125 der processes in the Standard Model [18, 19] or even a protophobic fifth force
126 mediated by a new 17 MeV boson X17 [20]. [Zhang and Miller: <https://www.sciencedirect.com/science/article/pii/S0370269321000010>](https://www.sciencedirect.com/science/article/pii/S0370269321000010)

128 0.1.2 Other Experiments

129 Since the ATOMKI measurements, several experiments have been initiated to
130 attempt to replicate the results and search for the hypothetical X17 particle.
131 [Here are a few with results. Could cite the ATOMKI review paper here.](#)

132 Two-arm e^+e^- spectrometer in Hanoi

133 The anomaly in ${}^8\text{Be}$ has been observed with $> 4\sigma$ confidence by a team at the
134 Hanoi University of Sciences for $E_p = 1225$ keV [21]. They built a two-arm
135 spectrometer in collaboration with ATOMKI and calibrated it using the 17.6 MeV
136 M1 transition. The results are shown in Figure 0.2.

137 Collisions at Nuclotron in Dubna

138 At the Joint Institute for Nuclear Research in Dubna, signal in the form of en-
139 hanced structures in the $\gamma\gamma$ spectra at ~ 17 and ~ 38 MeV invariant masses

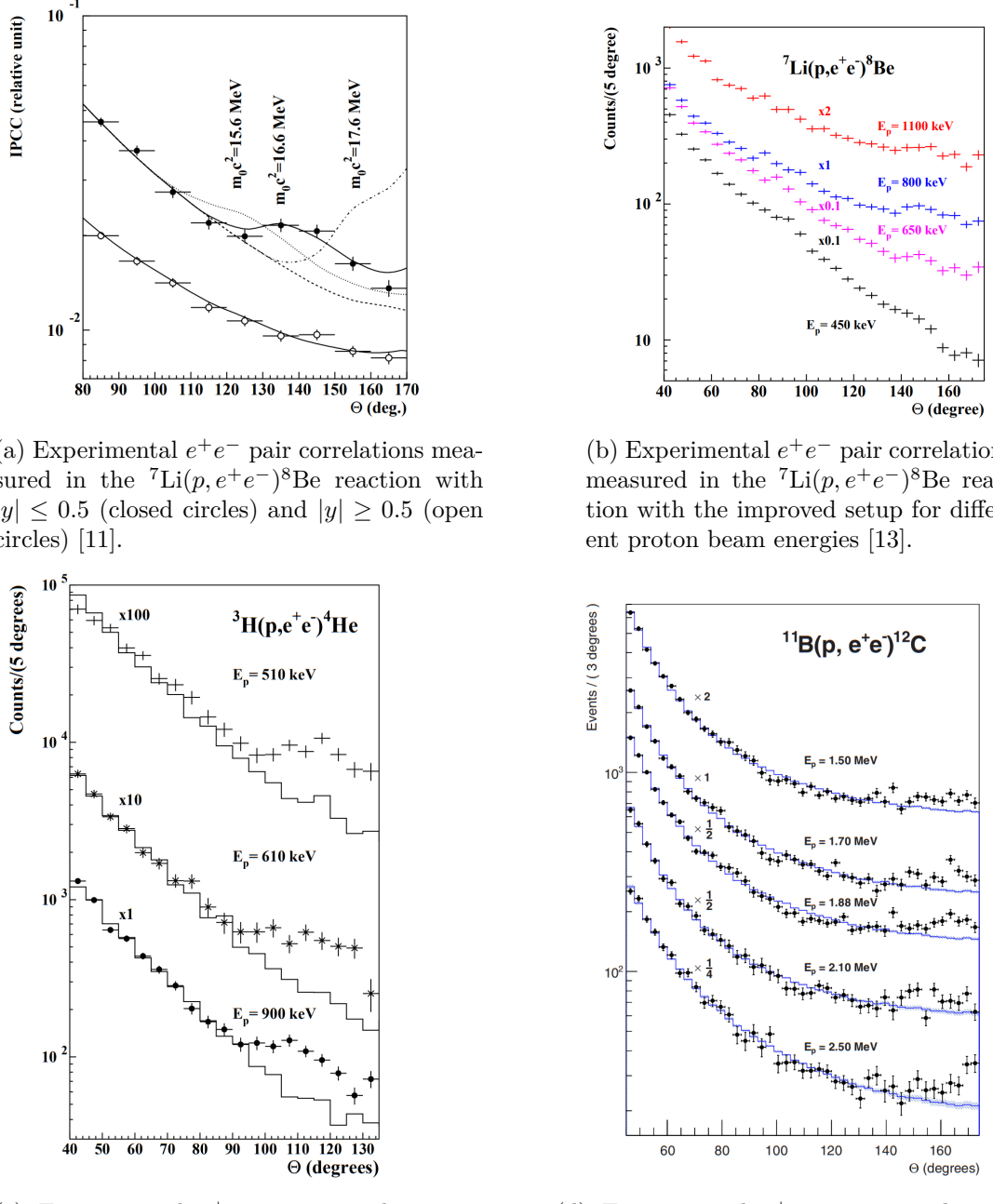


Figure 0.1: The ATOMKI anomalous IPC measured for different nuclei.

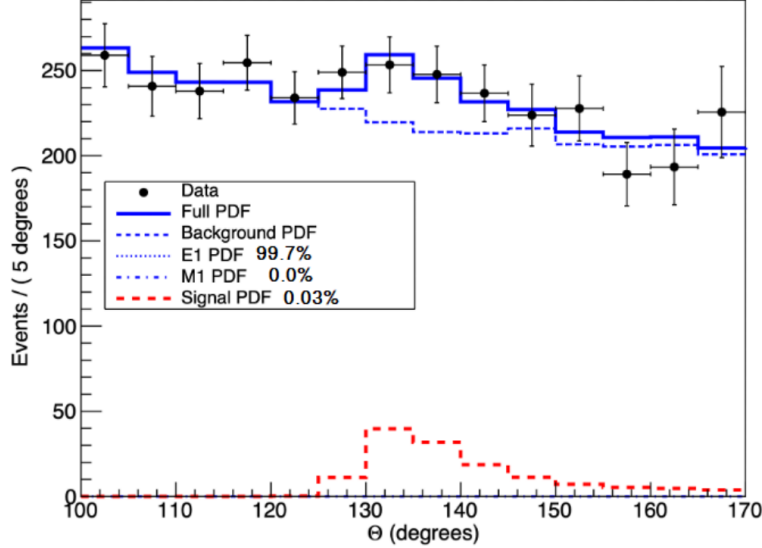


Figure 0.2: Results from the Hanoi spectrometer – angular e^+e^- pair correlations measured in the ${}^7\text{Li}(p, e^+e^-){}^8\text{Be}$ reaction at $E_p = 1225$ keV [21].

for $p + \text{C}$, $d + \text{C}$ and $d + \text{Cu}$ reactions at momenta 5.5, 2.75, and 3.83 GeV per nucleon [22]. Monte Carlo simulations support the conclusion that the signals are a consequence of a decay of unknown particles X17 and E38.

143 The MEG II (Muon Electron Gamma) experiment

144 Experiments using the ${}^7\text{Li}(p, e^+e^-){}^8\text{Be}$ reaction were carried out at the Paul Scherrer Institute with the MEG II superconducting solenoid spectrometer [23].
145 Analysis of the data with $E_p = 1080$ keV exciting both of the resonances (beam
146 fully stopping in the target) found no significant evidence supporting the X17
147 hypothesis, results are shown in Figure 0.3. An upper bound (at 90% confidence)
148 on the X17-to- γ branching ratio was set at $1.2 \cdot 10^{-5}$ for the 18.15 MeV state
149 (larger than the ratio $5.8 \cdot 10^{-6}$ obtained by ATOMKI in 2016). Could add their
150 90% C.L bounds figure also.
151

152 0.2 X17 Project at IEAP CTU

153 The aim of the X17 project at the Van der Graaff facility of the Institute of
154 Experimental and Applied Physics, Czech Technical University in Prague is to
155 repeat the original ATOMKI experiments with ${}^7\text{Li}$ and ${}^3\text{H}$ targets using an inde-
156 pendent e^+e^- spectrometer. In order to effectively measure the anomaly, we need
157 to reconstruct both the energy and the angular correlation of the e^+e^- pairs. The
158 spectrometer will use three layers of detectors to achieve this – Timepix 3 (Tpx3)
159 silicon pixel detector and Multi-Wire Proportional Chamber (MWPC) layers for
160 the angle reconstruction and a Time Projection Chamber (TPC) layer for the en-
161 ergy reconstruction. The schematics of the prepared detector is in Figure 0.4
162 Spectrometer CAD drawing (coordinates here or next chapter?). Cite some VdG
163 paper, mention grant? Using https://cernbox.cern.ch/pdf-viewer/public/rf0oU1nqVLN3acZ/LuzH_submitted.pdf.
164

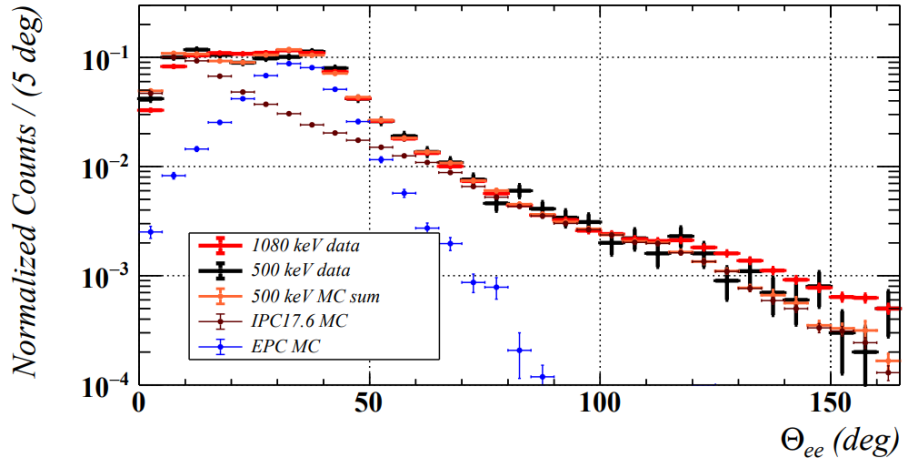


Figure 0.3: Results from the MEG II experiments – angular correlation of e^+e^- pairs with $E_{\text{sum}} \in [16, 20]$ MeV measured in the ${}^7\text{Li}(p, e^+e^-){}^8\text{Be}$ reaction with proton beam energies 500 and 1080 keV. The 500 keV dataset is fitted with Monte Carlo of both the IPC deexcitation and the EPC produced by gammas [23].

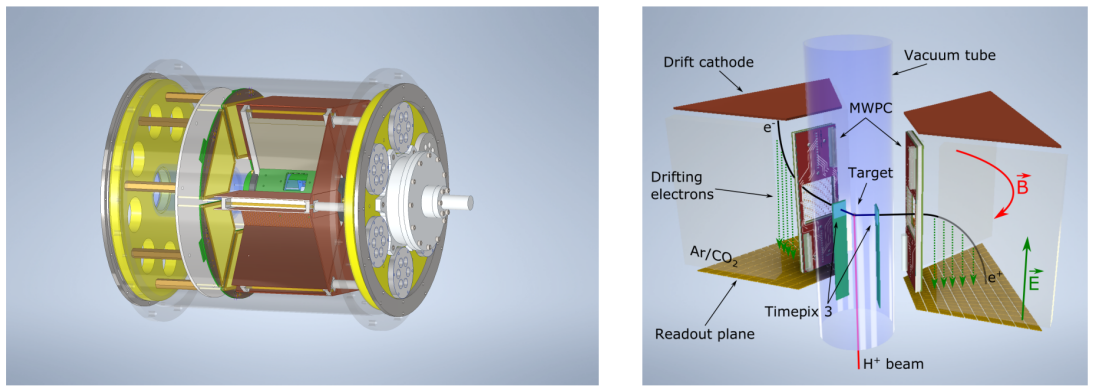


Figure 0.4: Schematics of the detector at the Van der Graaff facility at IEAP CTU.

165 The energy of e^+e^- pair produced in the reaction is given by the energy
166 available E_r in the reaction and can be distributed between them arbitrarily.
167 Nonetheless in the decay of the hypothetical X17 particle, electron and positron
168 should have similar energy and we can therefore use a disparity cut $|y| \leq 0.5$
169 for the disparity parameter (defined in Equation 0.1). Interesting events should
170 rarely have a particle with an energy below $E_r/4$ (roughly 4 MeV). Electrons with
171 such low energies are scattered significantly by even a thin layer of relatively light
172 material, for this reason the Tpx3 layer will be inside of the vacuum tube and the
173 tube will have a thinned aluminum segment or KaptonTM windows.

174 Tpx3 can measure (in each $55 \times 55 \mu\text{m}$ pixel of its 256×256 grid) time-of-arrival
175 (ToA) with 1.6 ns precision and time-over-threshold (ToT) which reflects the de-
176 posited energy. This potentially allows 3D tracking if we increase the chip thick-
177 ness at the cost of increased scattering. The layer can reconstruct the reaction
178 vertex and the angular correlation with high precision.

179 The layer of MWPCs with sensitive area $40 \times 38 \text{ mm}^2$ will be outside of
180 the beam pipe. It will provide an extra point on the particle trajectory which can
181 help with the estimation of the reaction vertex and improve the TPC performance
182 by providing its entry point.

183 The TPCs, which are a subject of this theses, are in a magnetic field of per-
184 manent magnets positioned between them and provide 3D track reconstruction
185 and subsequent momentum and particle identification (its charge, or even type
186 based on its stopping power). They avoid radiative losses thanks to the small
187 interaction with the incident particle. For the readout, triple Gas Electron Mul-
188 tiplier (GEM) will be used. The magnetic field layout in our TPCs is atypical –
189 orthogonal to the electric field inside the chamber, this is why we call them Or-
190 thogonal Fields TPC (OFTPC). Further details about our OFTPCs are provided
191 in section 1.3.

1. Time Projection Chamber

193 Using (2010 – a little old) <https://cds.cern.ch/record/1302071/files/CERN-PH-EP-2010-047.pdf>

195 A Time Projection Chamber (TPC) is a type of gaseous detector that uses
196 the drift in an electric field of free charges (electrons and cations, **also anions**
197 **if attachment is considered**) produced by an ionizing particle to reconstruct its
198 3D trajectory. When placed inside a magnetic field, the momentum of the incident
199 particle can be inferred from the curvature of its trajectory. Particle identification
200 is also possible using the ionization energy loss inside the TPC.

201 The original TPC used in the PEP-4 experiment at SLAC (Figure 1.1) was
202 a 2×2 m cylinder with a central cathode that produced a strong electric field,
203 making the ionization electrons drift towards one of the bases. The readout
204 consisted of MWPCs, where electrons are accelerated towards the anode wires
205 enough to further ionize the gas and cause an avalanche.

206 When a charged particle crosses the volume of a TPC, it loses energy by ex-
207 citation and ionization of the detector gas (**how much – from dE/dx + density**
208 **→ footnote?**). Most ionizing collision produce a single ionization electron, some-
209 times a few secondary electrons are produced close to the collision vertex. In
210 rare cases, the ionization electron has energy large enough to create a measurable
211 track, such an electron is called a δ -electron (**terminology, just like bellow – tech-**
212 **nically it's a (primary) ionization electron causing other (secondary) ionization**).
213 Penning transfer (collisions, light – factor 10 for gas gain in Ar/CO₂ viz PDG
214 CERN)?

215 CERES/NA45 – very inhomogeneous magnetic field

216 1.1 Charge transport in gases

217 1.1.1 Drift

218 Produced ionization electrons (**terminology – called ionization electrons in the**
219 **rest of the thesis**) are accelerated towards the readout by the electric field in-
220 side the chamber. At the same time, they lose speed by colliding with the gas
221 particles, quickly reaching a constant (for a given field \mathbf{E}, \mathbf{B}) mean drift velocity.
222 The electrons might be absorbed by electronegative impurities, such as halides
223 and oxygen.

224 In many gases (called "hot", e.g., Ar or CH₄), the drift velocity is much greater
225 than that of their thermal motion thanks to a high proportion of elastic collisions.
226 On the other hand, "cold" gases like CO₂ have a higher proportion of inelastic
227 collisions (e.g., thanks to the excitation of rotational and vibrational states) and
228 therefore much lower (**value? magnitude (implied)?**) drift velocity. (**def?**)

229 The ions produced by the ionization lose a significant portion of their energy
230 during each collision since their mass is close to the mass of the gas particles (**see**
231 **the source material – average energy loss during collision** $\Delta E = \frac{2m_i M}{(m_i + M)^2}$, **this way**
232 **it's more accurate**). This, together with their large collision cross section, makes
233 their drift velocity much smaller and their energy is close to thermal. Since their
234 momenta aren't randomized to such an extent during collisions, their diffusion

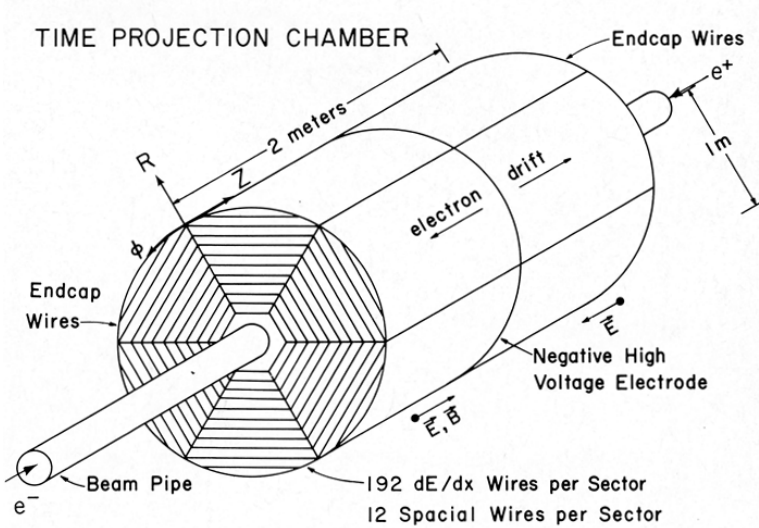


Figure 1.1: Schematic view of the PEP-4 TPC [24].

235 is smaller (more in the sense of distribution of positions, could move this to the
236 diffusion subsection).

237 The drift is also influenced by the magnetic field. Langevin derived a good
238 approximation for the drift velocity vector:

$$\mathbf{v}_d = \left(\frac{\mathbf{E}}{\|\mathbf{E}\|} + \omega\tau \frac{\mathbf{E} \times \mathbf{B}}{\|\mathbf{E}\| \|\mathbf{B}\|} + \omega^2\tau^2 \frac{\mathbf{E} \cdot \mathbf{B}}{\|\mathbf{E}\| \|\mathbf{B}\|} \cdot \frac{\mathbf{B}}{\|\mathbf{B}\|} \right) \frac{q\tau}{m(1 + \omega^2\tau^2)} \|\mathbf{E}\|, \quad (1.1)$$

239 where q is the charge of the particle, m is its mass, τ is the mean time between
240 collisions and $\omega = \frac{q}{m} \|\mathbf{B}\|$ is the Larmor frequency. In a standard TPC, \mathbf{E} is
241 nearly parallel to \mathbf{B} and the influence of the magnetic field on the drift is minimal.
242 The drift of ions is only negligibly influenced by the magnetic field ($\omega\tau \sim 10^{-4}$
243 is small due to the low drift velocity – better because it takes τ into account
244 and differs only by E/B ratio). Lorentz angle for orthogonal fields $\tan \psi = -\omega\tau$
245 (deviation from electric field) – maybe mention in the OFTPC section. Without
246 magnetic field, we can write

$$\mathbf{v}_d = \frac{q\tau}{m} \mathbf{E} = \mu \mathbf{E}, \quad (1.2)$$

247 where μ is called charge mobility.

248 1.1.2 Diffusion

249 Due to collisions a cloud of electrons or ions originating from the same point will
250 show a Gaussian density distribution at time t while drifting in the electric field
251 $\mathbf{E} = (0, 0, E_z)$:

$$\rho(x, y, z, t) = (4\pi Dt)^{-\frac{3}{2}} \exp \left(-\frac{x^2 + y^2 + (z - v_d t)^2}{4Dt} \right), \quad (1.3)$$

252 where the diffusion coefficient D can be expressed as

$$D = \frac{\lambda^2}{3\tau} = \frac{\lambda v_d}{3} = \frac{v_d^2 \tau}{3} = \frac{2\varepsilon\tau}{3m}, \quad (1.4)$$

253 where λ is the mean free path and ε the mean energy. The lateral diffusion width
254 σ_x after a drift distance L can be expressed as

$$\sigma_x^2 = 2Dt = \frac{4\varepsilon L}{3qE}. \quad (1.5)$$

255 The minimal diffusion width is given by the lowest possible energy of the particles
256 $\varepsilon_{\text{th}} = \frac{3}{2}kT$ (corresponding to thermal motion):

$$\sigma_{x,\min}^2 = \frac{2kTL}{qE}. \quad (1.6)$$

257 For electrons in "cold gases" (e.g., Ar/CO₂ mixture), the diffusion approaches
258 this limit up to a certain field intensity (~ 100 V/cm at 1 atm pressure)¹. In
259 reality, the transversal diffusion of electrons can differ significantly from their
260 longitudinal diffusion and simulations are necessary to get a precise result.

261 In most TPCs, the transversal (but not the longitudinal) diffusion is reduced
262 by the magnetic field, since it is parallel to the electric field and curves the dif-
263 fusing electrons around their mean trajectory:

$$\frac{D_T(B)}{D_T(0)} = \frac{1}{C + \omega^2 \tau_2^2}, \quad (1.7)$$

264 where C and τ_2 are parameters dependent on the gas used. At low intensity of
265 the magnetic field, we can use an approximation $C \approx 1$ and $\tau_2 \approx \tau$.

266 1.2 Readout

267 1.2.1 Multi-Wire Proportional Chamber

268 In most (2010 – almost all) TPCs operated in experiments Multi-Wire Proportion-
269 al Chamber (MWPC) was used for the readout. The electrons enter the cham-
270 ber through a cathode grid and get accelerated in the strong electric field towards
271 the thin anode wires and create a Townsend avalanche, multiplying the signal.
272 **Alternating with field wires?** The trajectory can be reconstructed using pulses
273 from each separate wire. Segmented cathode is also often used for the readout of
274 produced cations. **Gating grid (reduction of space charge effect, blocking backflow**
275 **of ions?, closed for electrons B=0, ΔV , static mode (loss of 25% el.) x opening on**
276 **trigger)? (gas amplification > 10000 required for good SNR, 100-200 ns shaping**
277 **time), figure?**

278 1.2.2 Gas Electron Multiplier

279 The Gas Electron Multiplier (GEM) is a thin metal-coated polymer sheet with
280 a high density of small holes. The amplification is achieved by applying voltage
281 on the metal layers, creating a strong electric field inside the holes and causing
282 avalanches. Double or triple stack of GEMs is usually used to create a sufficient
283 gain. From the last foil, the electrons drift to a segmented anode where the signal
284 is read. The backflow of cations is reduced compared to MWPC. An example
285 simulation of an avalanche inside GEM is shown in Figure 1.2. **Parameters?**

¹For us 0.45 mm, quite close to the actual diffusion 0.5-0.7 mm.

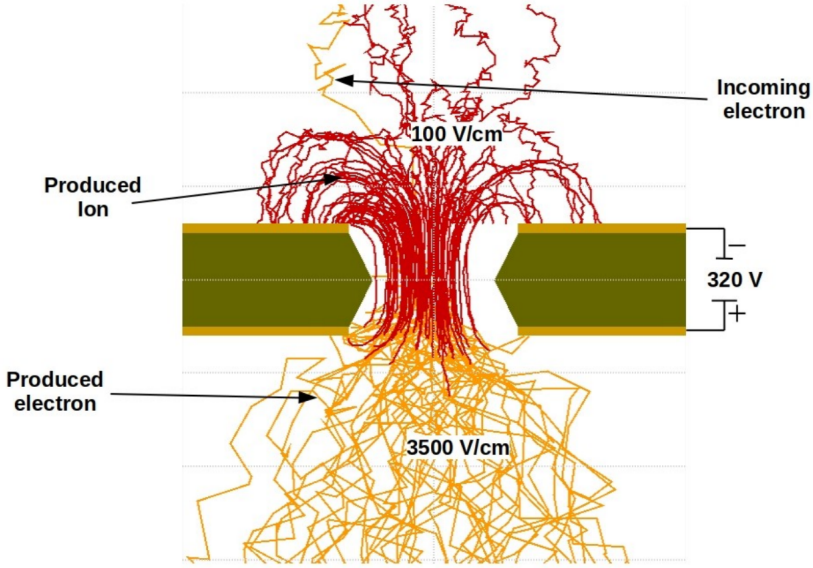


Figure 1.2: Garfield simulation of an avalanche in a GEM hole [25].

1.2.3 Micromegas

In a MICRO-MEsh GAseous Structure (Micromegas) electrons pass through a fine mesh (made out of very thin wires) into the narrow amplification gap where they are multiplied in the high field and read as signal on the segmented anode. Very high field ($30\text{-}80 \text{ kV/cm}^2$) is necessary to achieve sufficient gain. Cation backflow is heavily suppressed by the mesh.

1.2.4 Parallel Plate Chamber

..., micowell?

1.3 Orthogonal Fields TPC at IEAP CTU

At IEAP CTU, we are going to use six identical atypical TPCs with inhomogeneous toroidal magnetic field orthogonal to the electric field, hereafter referred to as Orthogonal Fields TPC (OFTPC). It has the shape of isosceles trapezoidal prism 16 centimeters high with triple-GEM readout on one of its bases. Dimensions of the OFTPC are discussed in detail in section 1.3.2 below. Throughout this thesis, we assume a uniform electric field along the z axis with $E_z = -400 \text{ V/cm}$. Gas mixture used in the detector (70/30) and its effect – some graph with the mixture.

1.3.1 Motivation and Associated Challenges

The reasons for the unusual field layout are mostly cost related:

- we use permanent magnets instead of a solenoid and parallel fields are difficult to accomplish this way,
- granularity of the TPC readout is limited in order to fit one SAMPA/SRS hybrid in each sector – parallel fields would bend the trajectories parallel

309 to the readout requiring more pads and different architecture.

310 In this thesis, we will show that such a setup can reach a similar energy resolution
311 as common cylindrical TPCs while reducing cost.

312 The layout introduces two complications to the track reconstruction – the
313 trajectory in inhomogeneous field is not circular and the drift is distorted by
314 the magnetic field (see Equation 1.1, in our case $\omega\tau \approx 0.08$ for 0.3 T assuming
315 $\mu \approx 0.25 \text{ T}^{-1}$, varies inside the detector). The diffusion in such setup is larger
316 since parallel orientation reduces diffusion by curling the electrons in the x - y
317 direction (see Equation 1.7) but for our relatively weak magnetic field and short
318 drift distance the difference is negligible.

319 1.3.2 Coordinate Systems and Dimensions

320 In order to describe events in our detector, we use three distinct spaces: the de-
321 tector space \mathcal{D} , the readout space \mathcal{R} and the pad space \mathcal{P} . Each space is later
322 used to represent ionization electrons at different stages of the detection process:
323 their creation in the gas, their final position when hitting the readout plane, and
324 finally their representation in the discrete pad space.

325 Detector Space

326 The detector space \mathcal{D} represents the physical space of our detector. We de-
327 scribe it using Cartesian coordinates (x, y, z) . The z -axis is the detector's axis of
328 symmetry, with its negative direction aligned with the proton beam. The origin
329 $(0, 0, 0)$ is located at the center of the irradiated target. The positive x -axis passes
330 through the center of one the OFTPCs along the intersection of its two planes
331 of symmetry. The y -axis is then chosen to maintain a right-handed coordinate
332 system.

333 Since the detector has a hexagonal symmetry, we use only one of its sectors
334 in this work – the first sector $\mathcal{D}_1 \subset \mathcal{D}$ which is defined by the condition:

$$(x, y, z) \in \mathcal{D}_1 \Leftrightarrow |y| \leq x \tan \frac{\pi}{6}. \quad (1.8)$$

335 Simulations in this sector can be applied to all sectors by rotating the coordinates
336 accordingly. The volume of the OFTPC in this sector, which has the shape of
337 a trapezoidal prism, has these boundaries:

$$x \in [x_{\min}, x_{\max}] = [6.51, 14.61] \text{ cm}, \quad (1.9)$$

$$z \in [z_{\min}, z_{\max}] = [-8, 8] \text{ cm}, \quad (1.10)$$

$$y_{\max}(x_{\min}) = -y_{\min}(x_{\min}) = 2.75 \text{ cm}, \quad (1.11)$$

$$y_{\max}(x_{\max}) = -y_{\min}(x_{\max}) = 7.45 \text{ cm}, \quad (1.12)$$

338 where $y_{\max}(x)$ is the maximal value of the y -coordinate for a given x . The read-
339 out is located at $z = 8$ cm; for some purposes, we also define the distance to
340 the readout $d_r = 8 \text{ cm} - z$ as an alternative to the z -coordinate. Keeping this
341 paragraph as it is because the OFTPC volume is distinct from the first sector
342 and some parts of this thesis use the space beyond this volume.

343 We also use spherical coordinates (r, θ, φ) with θ measured relative to the xy
344 plane.

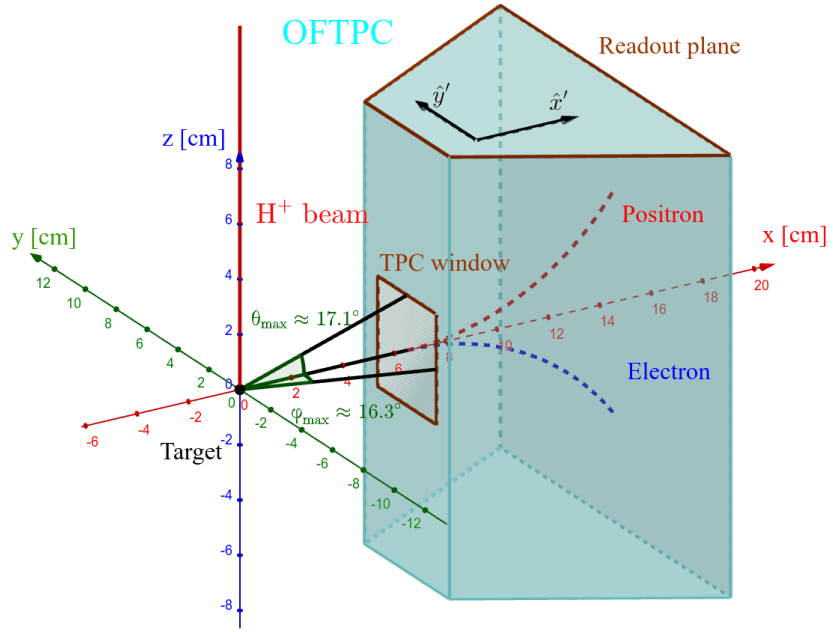


Figure 1.3: Schematics of the first sector OFTPC with detector space coordinates.

345 Readout Space

346 The readout space \mathcal{R} represents the drift time and final positions of ionization
 347 electrons as measured by an ideal continuous readout. We describe it using
 348 coordinates (x', y', t) , where x' and y' correspond to the detector coordinates at
 349 the readout plane ($z = 8 \text{ cm}$). Currently not entirely sure how to put this
 350 into a figure since only x' and y' correspond to the detector coordinates, it will
 351 make more sense when visualizing the map. The drift time t is approximately
 352 proportional to d_r .

353 Pad Space

354 The pad space \mathcal{P} represents the time bin and pad number of ionization electrons
 355 as measured by an ideal discrete readout:

$$\mathcal{P} = \{(n_{\text{pad}}, n_t) \in \mathbb{N}^2 \mid n_{\text{pad}} \leq 128\}. \quad (1.13)$$

356 Technically both values can be zero as defined in the code (max channel 127).
 357 It is not really a subspace of \mathcal{R} but there is a mapping from \mathcal{R} to \mathcal{P} . It is a
 358 discretization of a part of \mathcal{R} , the mapping can be adjusted depending on the sim-
 359 ulation. If we assume uniform electric field there will be gaps, we don't use gaps
 360 in the reconstruction since the electrons should be pulled towards the pads.

361 The readout of the OFTPC will consist (is the design final?) of 128 rectangular
 362 pads arranged in a staggered pattern. Parameters of the pad layout are shown
 363 in Figure 1.4. The bottom left corner of n -th pad has coordinates $(x_{1,n}, y_{1,n})$,
 364 the top right $(x_{2,n}, y_{2,n})$ and its center has coordinates $(x_{c,n}, y_{c,n})$. The gap
 365 between neighboring pads is $g = 0.08 \text{ cm}$. Time will be read out with 100 ns
 366 intervals (details?). Could also describe pad-related functions.

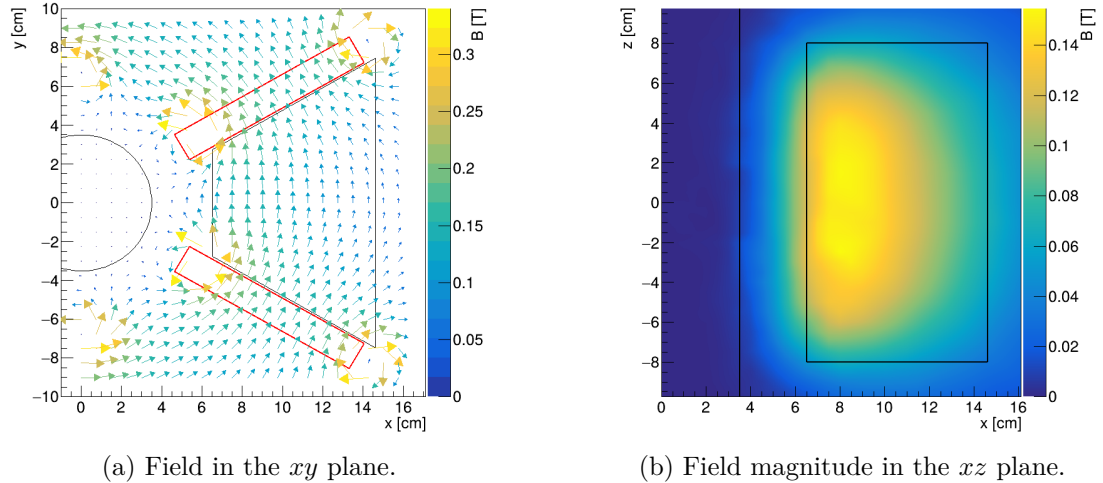


Figure 1.5: Magnetic field simulation results. The OFTPC volume and the vacuum tube are marked with black lines, the magnets are marked with red lines. The coordinates of the magnets from the CAD drawing seem to be 9/10 of the ones from the magnetic simulation (confirm and fix).

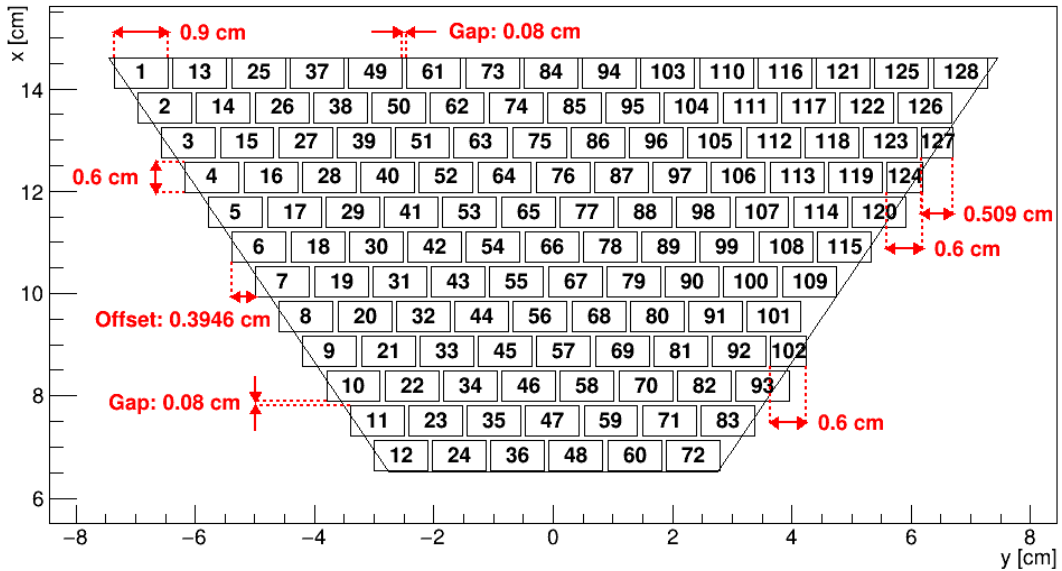


Figure 1.4: Pad layout of the OFTPC and its parameters. Pads 102, 124 and 127 are irregular, the rest has the same dimensions.

367 1.3.3 Magnetic Field Simulation

368 The magnetic field inside our detector is produced by six permanent magnets. It
 369 was simulated using Ansys Maxwell ([citation?](#)) which gives us values on a regular
 370 grid. Visualization of the magnetic field is shown in Figure 1.5. Whenever we
 371 need to work with values outside this grid, we use trilinear interpolation described
 372 below.

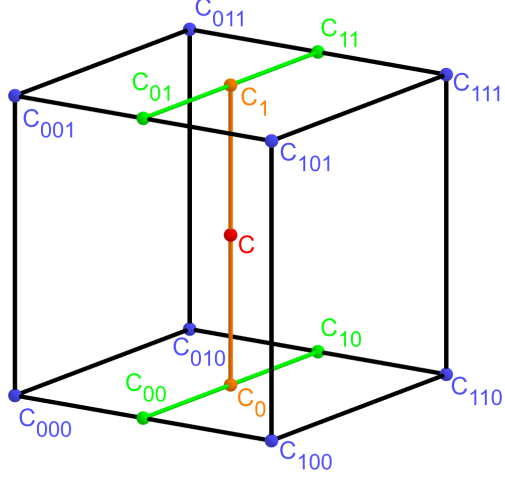


Figure 1.6: Visualization of trilinear interpolation as a composition of linear interpolations. **Image drawn in GeoGebra and inspired by a similar image on Wikipedia (which looks a bit worse) – is credit necessary?**

373 Trilinear Interpolation

374 Trilinear interpolation is a 3D generalization of linear interpolation. It can be
 375 used to interpolate a function whose values are known on a regular grid with
 376 rectangular prism cells. We use this simple method for interpolating the magnetic
 377 field, and it is later used in Section 3.2.1 to interpolate the Ionization Electron
 378 Map, a key component of our track reconstruction algorithm. In both cases, we
 379 use a regular cubic grid (apparently it is also called a [Cartesian grid](#)).

380 Could put a paragraph about linear interpolation here if it is not clear from
 381 the equations below.

382 Let us consider a cell of our regular grid (a cube) with an edge of length a
 383 containing the point $\mathbf{C} = (x, y, z)$ where we want to interpolate a function
 384 $f: \mathbb{R}^3 \rightarrow \mathbb{R}$. We know the values of this function at the vertices of the cell
 385 $\mathbf{C}_{ijk} = (x_0 + ia, y_0 + ja, z_0 + ka)$, where $i, j, k \in \{0, 1\}$ are indices. We also define
 386 the points $\mathbf{C}_{ij} = (x, y_0 + ia, z_0 + ja)$ and $\mathbf{C}_i = (x, y, z_0 + ia)$. Then the interpolated
 387 value $\hat{f}(\mathbf{C})$ can be calculated as a composition of three linear interpolations (see
 388 Figure 1.6):

$$\hat{f}(\mathbf{C}_{ij}) = (1 - x_d) f(\mathbf{C}_{0ij}) + x_d f(\mathbf{C}_{1ij}), \quad (1.14)$$

$$\hat{f}(\mathbf{C}_i) = (1 - y_d) \hat{f}(\mathbf{C}_{0i}) + y_d \hat{f}(\mathbf{C}_{1i}), \quad (1.15)$$

$$\hat{f}(\mathbf{C}) = (1 - z_d) \hat{f}(\mathbf{C}_0) + z_d \hat{f}(\mathbf{C}_1), \quad (1.16)$$

389 where x_d , y_d , and z_d are given as follows:

$$x_d = \frac{x - x_0}{a}, \quad y_d = \frac{y - y_0}{a}, \quad z_d = \frac{z - z_0}{a}. \quad (1.17)$$

390 We can also write

$$\hat{f}(\mathbf{C}) = \sum_{i,j,k \in \{0,1\}} t_x^i t_y^j t_z^k f(\mathbf{C}_{ijk}), \quad (1.18)$$

$$t_\alpha \stackrel{\text{def}}{=} \begin{pmatrix} t_\alpha^0 \\ t_\alpha^1 \end{pmatrix} = \begin{pmatrix} 1 - \alpha_d \\ \alpha_d \end{pmatrix}, \quad (1.19)$$

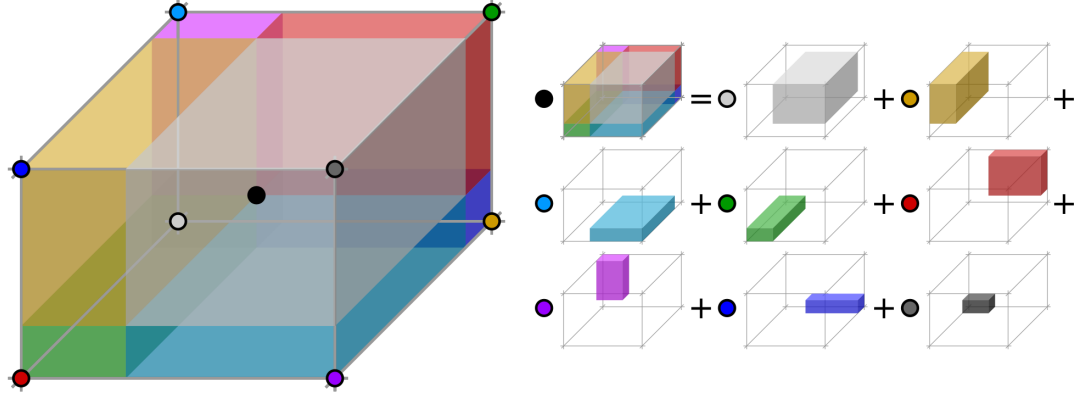


Figure 1.7: Geometric interpretation of trilinear interpolation. The colored dots represent the values in given points and the colored boxes represent the volume by which the corresponding values are multiplied. The black dot represents the interpolated value [26].

391 where $\alpha \in \{x, y, z\}$ is an index. This gives a nice geometric interpretation to the
 392 trilinear interpolation as shown in Figure 1.7. Furthermore, we can write $\hat{f}(\mathbf{C})$
 393 as a polynomial:

$$\hat{f}(\mathbf{C}) = \sum_{\alpha, \beta, \gamma \in \{0, 1\}} \sum_{i=0}^{\alpha} \sum_{j=0}^{\beta} \sum_{k=0}^{\gamma} (-1)^{(\alpha-i) + (\beta-j) + (\gamma-k)} f(\mathbf{C}_{ijk}) x_d^{\alpha} y_d^{\beta} z_d^{\gamma}. \quad (1.20)$$

394 We take advantage of this form when generalizing trilinear interpolation to irreg-
 395 ular grid in section 3.2.2.

396 Maybe a citation here, although I am not sure it is necessary since it could
 397 be considered common knowledge. The last two equations are my own. Maybe
 398 x_0 , etc. should be explicitly described.

399 2. Track Simulation

400 In order to develop and test the reconstruction algorithm, electron and positron
401 tracks are simulated inside the first sector \mathcal{D}_1 of our detector (see Section 1.3.2)
402 with different initial parameters. Two approaches are currently used to simulate
403 tracks, each of them for different purpose.

404 The **Microscopic Simulation** uses the Garfield++ toolkit [1]. Within this
405 toolkit, the High Energy Electro-Dynamics (HEED) program [27] is used to simu-
406 late the primary particle and the class *AvalancheMicroscopic* to simulate the drift
407 of secondary electrons created by ionization in the gas. This is the most precise
408 and time-consuming simulation used; our current goal is to be able to successfully
409 reconstruct its results and determine our best-case energy resolution.

410 The **Runge-Kutta Simulation** uses the 4th order Runge-Kutta numerical
411 integration ([add citation for Runge-Kutta](#)) to simulate the trajectory of the pri-
412 mary particle in the electromagnetic field inside the detector. It is relatively
413 fast since it does not simulate the secondary particles. It is used as part of our
414 reconstruction algorithm and for testing some parts of the reconstruction.

415 All of these simulations require the knowledge of the electromagnetic field
416 inside the detector. A uniform electric field of $400 \text{ V}\cdot\text{cm}^{-1}$ is assumed. The mag-
417 netic field was simulated in Maxwell (see Section 1.3.3). [add citation](#)

418 [Single track in positive x direction or initial parameter randomization. Im-](#)
419 [portance of gas composition, used gas compositions.](#)

420 2.1 Microscopic Simulation

421 The microscopic simulation, the most detailed simulation used in this work, is
422 performed using the Garfield++ toolkit [1].

423 The electron transport properties are simulated using the program Mag-
424 boltz ([Add citation](#)). Two different gas mixtures were used: 90% Ar + 10% CO₂
425 and 70% Ar + 30% CO₂. The second mixture will be used in our detector.
426 The temperature is set to 20 °C, the pressure is atmospheric.

427 The primary track is simulated using the program HEED [27], which is an
428 implementation of the photo-absorption ionization model. This program pro-
429 vides the parameters of ionizing collisions. HEED can also be used to simulate
430 the transport of delta electrons; we do not account for these in the current sim-
431 ulation but plan to include them in the future. The photons created in the atomic
432 relaxation cascade ([fluorescence reabsorption, ?](#)) are also not simulated.

433 Finally, we use the microscopic tracking provided by the class *AvalancheMicro-*
434 *scopic* to simulate the drift of the ionization electrons. Each electron is followed
435 from collision to collision using the equation of motion and the collision rates
436 calculated by Magboltz.

437 [First simulated track in the z direction should be described in detail here \(own](#)
438 [subsection?\). Figures.](#)

439 [Add more detailed and better description of HEED, and microscopic tracking](#)
440 [\(each their own subsection?\). Could also mention Monte Carlo \(requires gas file](#)
441 [generation - Magboltz\) and Runge-Kutta simulation implemented in Garfield,](#)

442 why we don't use them (another subsection? rename the section to Garfield++
443 simulation and mention all relevant parts?).

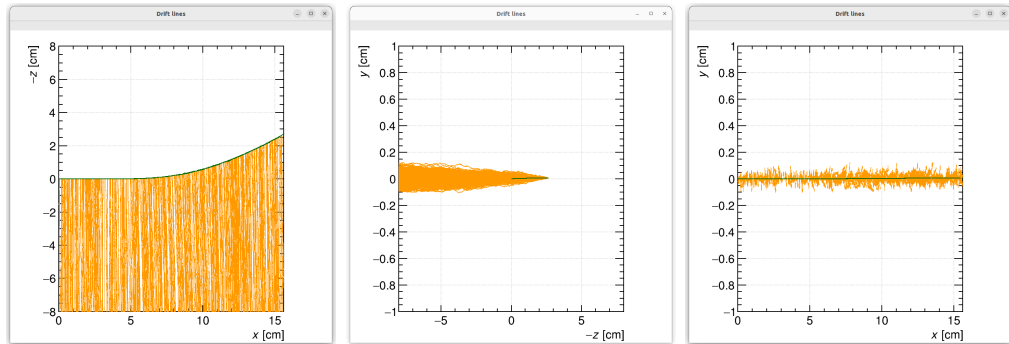


Figure 2.1: Example of a simulated electron track in 70 % argon and 30 % CO₂ atmosphere (on the left). Swap for better images, better zoom. Explain drift lines, primary particle.

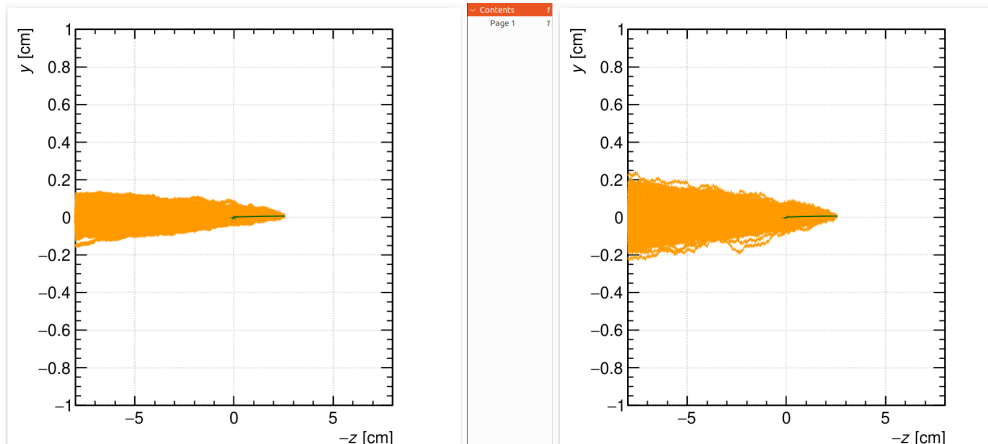


Figure 2.2: Comparison of diffusion in a simulated electron track in 70 % argon, 30 % CO₂ atmosphere and in 90 % argon, 10 % CO₂ atmosphere (on the right). Swap for better image, better zoom. Or put the same pictures for both comparisons in one subfigure, etc. Describe better.

444 2.2 Runge-Kutta Simulation

445 Trajectory simulation with 4th order Runge-Kutta. Relativistic equation that is
446 numerically integrated by the algorithm.

3. Track Reconstruction

In the first stage of the reconstruction algorithm, we reconstruct the track of a primary particle (either an electron or a positron). The result of this step is then used to determine the energy of the particle (Section 4).

The **Reconstruction Assuming Steady Drift** uses the standard TPC approach. With parallel fields, the drift inside a uniform electric field remains undistorted (reference to some future part of the TPC chapter). Therefore, we only need to reconstruct the z -coordinate from the drift time using the known drift velocity. We also assume that the readout coordinates (x', y', t) are known exactly, neglecting the pads and time bins.

Reconstruction using the **Ionization Electron Map** (from now on referred to as *the map*) uses a simulation of the drift of secondary (ionization) electrons within the detector volume. This simulation can then be used to interpolate the initial position of the secondary electrons. First attempts neglect the pads.

We use the map for reconstruction in two different ways. The first one uses gradient descent search along with trilinear interpolation (see Section 1.3.3) of the map. The second method uses interpolation on the irregular inverse grid with a linear polynomial.

The **Discrete Reconstruction** uses the map; instead of reconstructing the exact position of each electron, we reconstruct the center of each hit pad with the time corresponding to the midpoint of the time bin. The electron count in each TPC bin (consisting of the pad and the time bin) serves as the charge value, which is then used as a weight in the energy reconstruction fit.

3.1 Reconstruction Assuming Steady Drift

As the first step, we decided to try to reconstruct an electron track with a special set of initial parameters. The origin of the particle is given by the origin of our coordinate system. The initial direction is given by the positive x -axis. This means the magnetic field of our detector is perpendicular to the momentum of the particle at all times, and we can reduce the problem to two-dimensional space. As an example, we use a track simulated using the microscopic simulation (see Section 2.1) with a kinetic energy of 8 MeV. The gas composition used in this simulation is 90% Ar + 10% CO₂. Might be better to describe this track in Section 2.1.

In this approach to the reconstruction of the track, we decided to use the common method used in a standard TPC. This will allow us to explore the significance of the atypical behavior in our OFTPC. Additionally, we assume the readout is continuous to further simplify the problem. In this approximation, we reconstruct the initial position of each ionization electron.

The reconstruction is then defined by the following relations between the coordinates of the detector space and the readout space (see Section 1.3.2):

$$x = x', \quad (3.1)$$

$$y = y', \quad (3.2)$$

$$z = v_d t, \quad (3.3)$$

487 where v_d is the drift velocity of electrons in the given gas mixture. At a phe-
 488 nomenological level, this velocity can be considered as a function of the electric
 489 field \mathbf{E} and the magnetic field \mathbf{B} :

$$v_d = v_d(\mathbf{E}, \mathbf{B}). \quad (3.4)$$

490 Equation taken from Garfield user manual. The Garfield++ toolkit uses this
 491 fact to accelerate their drift simulation with non-microscopic approaches (could
 492 mention in the simulation chapter). Since we assume a uniform electric field in
 493 our detector and we want to neglect the effect of our unusual magnetic field, we
 494 consider the drift velocity to be constant in this scenario. We then approximate
 495 this velocity by fitting the dependence $z(t)$ taken from the simulated ionization
 496 electrons. This is in one of the provisional figures. Also, this description is
 497 not completely accurate; in reality, we fit $t1:8-y0$ with $a1*x+a0$ and then invert
 498 this and use $8-y0 = b1*t1+b0$ (old coordinates); $b1=1/a1$ functions as the drift
 499 velocity. Maybe also define this 8-z variable as an alternative to z in Section 1.3.2
 500 and then use it when correcting this.

501 Later, in a commit after this, I plotted some residues (provisional figure),
 502 which could be useful, but for some reason they are residuals from a spline fit of
 503 the track?! Probably redo this without the spline fit; just explore the difference
 504 in individual points.

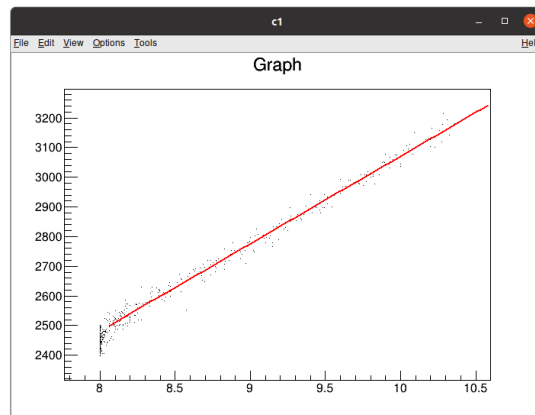


Figure 3.1: Dependence of the drift time on the z coordinate in 90 % argon and 10 % CO₂ atmosphere, fitted with a linear function. The fitted function gives us the average drift velocity in the gas and can be used for rough reconstruction in our TPC. Swap for better image with axis labels, etc. Maybe write the fitted equation.

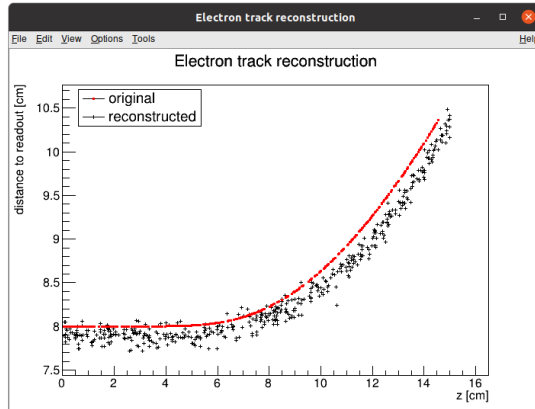


Figure 3.2: First attempt at a track reconstruction using only the drift velocity. This approach works well in a standard TPC (ideally cite some source?). 90 % argon and 10 % CO₂ atmosphere. Swap for better image, correct coordinates.

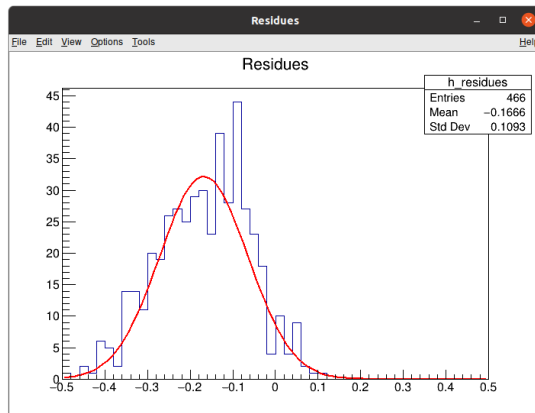


Figure 3.3: First attempt at a track reconstruction using only the drift velocity, residues. Swap for better image, correct coordinates. What's causing the shift? Explain details.

505 3.2 Ionization Electron Map

506 Inside an OFTPC, the drift of the secondary (ionization) electrons is significantly
507 affected by its magnetic field (pictures of the distortion later, the effect is bigger
508 for the 90/10 composition.). We need to take this into account for accurate
509 reconstruction. In the first approximation, we assume a continuous readout (i.e.,
510 we neglect pads). We can then reconstruct the original position of each ionization
511 electron using its readout coordinates. For this purpose, we use the ionization
512 electron map.

513 The ionization electron map represents a mapping from the detector space
514 to the readout space (see Section 1.3.2). It tells us what readout coordinates
515 (x', y', t) we can expect on average for an ionization electron created at the detec-
516 tor coordinates (x, y, z). More precisely it is a mapping to the distributions on
517 the readout space; we can simplify this as only the means $\bar{\mathcal{M}}$ and the covariance

518 matrices \mathcal{M}_{cov} , assuming Gaussian distribution.

$$\mathcal{M} : \mathcal{D} \longrightarrow \mathcal{R}, (x, y, z) \longmapsto (x', y', t). \quad (3.5)$$

519 To get an approximation of this mapping, we simulate the drift of ionization elec-
 520 trons generated on a regular grid inside the volume of our OFTPC¹. It is also
 521 useful to simulate multiple (100 in our case) electrons originating from the same
 522 position so we can get a better information about the average drift and its vari-
 523 ance. In order to get more accurate results, we use the microscopic simulation of
 524 these electrons described in Section 2.1. When evaluating the map inside the grid,
 525 we use trilinear interpolation (see Section 1.3.3). From now on, we will denote
 526 this interpolated simulation with the same symbol \mathcal{M} .

527 Finally, we need to invert the map to get the original detector coordinates
 528 (x, y, z) for the given readout coordinates (x', y', t) . In our case, we can reason-
 529 ably assume that the mapping $\overline{\mathcal{M}}$ is one-to-one (as seen in the simulations). We
 530 implemented two methods for this purpose: the gradient descent search (Sec-
 531 tion 3.2.1) and interpolation on the inverse grid (Section 3.2.2).

532 The simulation of the map is a computationally heavy task. For this reason,
 533 we use the MetaCentrum grid [3] to parallelize needed calculations. At first, this
 534 was done by evenly distributing the simulated electrons across the individual jobs
 535 in a simulation with only one electron per vertex in the regular grid with a spacing
 536 of one centimeter.

537 Later, a more efficient approach was implemented, accounting for the varying
 538 lengths of the drift of individual electrons. If we index the electrons in the order
 539 of increasing coordinates y, x, z ([picture?](#)), we can express the number n_l of full
 540 XY layers (i.e., electrons with the same z coordinate) of electrons with index less
 541 than or equal to i

$$n_l(i) = \left\lfloor \frac{i}{n_{xy}} \right\rfloor, \quad (3.6)$$

542 where n_{xy} is the number of electrons in each XY layer calculated simply by count-
 543 ing the electrons that satisfy boundary conditions for x and y . **These conditions**
 544 **should be mentioned above; sector condition + maximal x value.** The number of
 545 electrons remaining in the top layer is then

$$n_r(i) = i \bmod n_{xy}. \quad (3.7)$$

546 Finally, we can calculate the sum of the drift gaps of electrons up to index i

$$d_{\text{sum}} = (z_{\max} - z_{\min})n_{xy}n_l - \frac{n_l(n_l - 1)}{2}n_{xy}l + n_r(z_{\max} - z_{\min} - n_l l). \quad (3.8)$$

547 We then use a binary search algorithm to find the maximum index i such that
 548 the value of this sum is less than the fraction $\frac{\text{job id}}{\max \text{ job id}}$ of the total sum. This way
 549 we obtain the minimal and the maximal index of electrons simulated in the given
 550 job. **The spacing l should be probably defined above + picture of the simulating**
 551 **grid (1 layer). zmin zmax also**

552 After the simulation of the map, we calculate the mean readout coordinates
 553 assuming Gaussian distribution (i.e., we use averages). We also calculate standard

¹we do not take the detector walls into account and simulate even outside of the OFTPC which lets us interpolate even close to the walls

554 deviations in a later commit, should be upgraded to the covariance matrix. We
555 never actually plotted the distributions we get when simulating the same electron
556 multiple times, so we do not know if our assumptions are accurate (could also
557 run some statistical test to see how well the Gaussian distribution fits).

558 The obtained map is then stored in a custom class template *Field*, could
559 expand on that. Maybe earlier, since the same template is used for the magnetic
560 field.

561 Could insert a table here describing all 4 simulations of the map (gas composi-
562 tion, spacing, etc.). Simulation inside of one sector (at first double angle). Extra
563 space on the sensor. Edge cases not taken into account (TPC wall). Using qsub
564 (not sure if important). Add plots of distortion of the coordinates. Could also do
565 these plots in a different way (e.g., drawing all the endpoints of each ionization
566 electron or some error ellipse plot).

567

568 Images to add (comparison of both simulations):

- 569 • 3D visualization of the map, simulation example
- 570 • z vs. t plot
- 571 • XY plane distortion for different z values; with arrows and error bars, for
572 all z -layers with different colors
- 573 • XZ plane ($y = 0$) distortion in x (maybe not necessary?)
- 574 • XT plot ($y = 0$) showing (small) distortion in drift times

575

576 More images:

- 577 • Residuals of the continuous readout reconstruction.

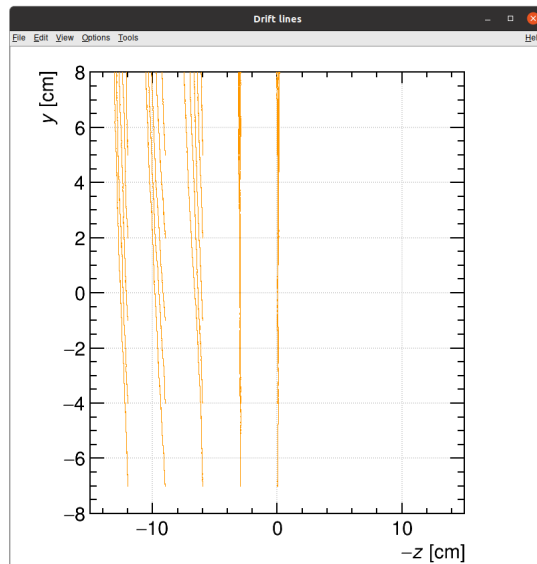


Figure 3.4: Example of map generation. Swap for better image, correct coordinates.

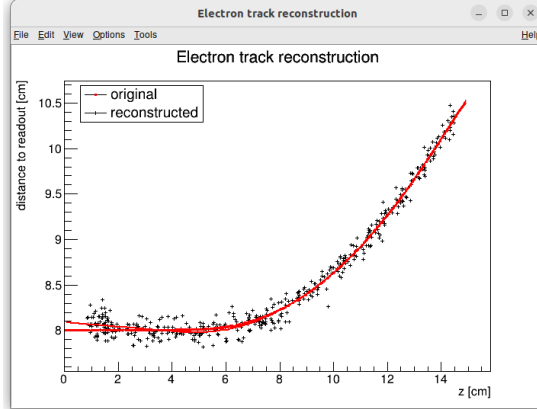


Figure 3.5: Example reconstruction with the map. Swap for better image, correct coordinates.

578 3.2.1 Gradient Descent Search

579 The first implemented method of reconstruction uses a gradient descent search
 580 to calculate an inversion of the map $\bar{\mathcal{M}}$ in a given point. Gradient descent is
 581 an iterative minimization algorithm for multivariate functions. Let $R \in \mathcal{R}$ be
 582 a point in the readout space; we want to find a point $D = (x, y, z) \in \mathcal{D}$ in
 583 the detector space such that

$$584 \quad \bar{\mathcal{M}}(D) = R = (x'_R, y'_R, t_R). \quad (3.9)$$

584 We define a function f_R in the readout space as a distance in this space:

$$f_R(x', y', t) = \sqrt{(x' - x'_R)^2 + (y' - y'_R)^2 + v_d^2(t - t_R)^2}, \quad (3.10)$$

585 where v_d is an approximation of the drift velocity in the TPC, obtained from
 586 the reconstruction in Section 3.1 (there will be an image with the linear fit there).

587 We make an initial guess (actually in the original code we just take $z = 0$):

$$D_0 = (x'_R, y'_R, v_d t). \quad (3.11)$$

588 Assuming we have the n -th estimate D_n , we calculate the i -th component of
 589 the gradient of $f_R \circ \bar{\mathcal{M}}$ numerically using central differences:

$$[\nabla(f_R \circ \bar{\mathcal{M}})]^i(D_n) \approx \frac{f_R(\bar{\mathcal{M}}(D_n + s \cdot e^i)) - f_R(\bar{\mathcal{M}}(D_n - s \cdot e^i))}{2s}, \quad (3.12)$$

590 where $e^i \in \mathcal{D}$ is the i -th coordinate vector and s is the step size. The step size
 591 should be sufficiently small; initially, we set it as a fraction of the map's grid
 592 spacing $s = \frac{l}{10}$. During the minimization, we check that $f_R(\bar{\mathcal{M}}(D_n)) < 10s$
 593 at all times. When using trilinear interpolation, it would be more efficient to
 594 calculate the gradient explicitly (\pm same result). This could be implemented
 595 inside the *Field* template class. The next iteration can be calculated as follows:

$$D_{n+1} = D_n - \gamma \nabla(f_R \circ \bar{\mathcal{M}})(D_n), \quad (3.13)$$

596 where $\gamma \in \mathbb{R}^+$ is the damping coefficient. It should be set to a small enough
 597 value to ensure convergence, but large enough for sufficient converging speed.

598 The minimization stops either when the error $f_R(\bar{\mathcal{M}}(D_n))$ drops below a specified
 599 value or when the number of iterations exceeds a certain limit (in this case,
 600 a message is printed into the console). The parameters of this method can be
 601 further optimized (e.g., a better choice of γ , gradient computation); instead, we
 602 later decided to use the interpolation on the inverse grid described in the next
 603 section.

604 Measure reconstruction duration and compare it with the inverse grid inter-
 605 polation? Also compare the result? Not sure if this has to be cited.

606 3.2.2 Interpolation on the Inverse Grid

607 Interpolating between known points in the readout space. Gaussian elimina-
 608 tion, multivariate polynomial. Benefits compared to the gradient descent search
 609 method (one-time computation for the whole map is easy to achieve if needed).

610 The currently used baseline reconstruction method is the interpolation on
 611 the inverse grid. Rather than attempting to invert the trilinearly interpolated
 612 map as in the previous section, we take advantage of the fact that the map $\bar{\mathcal{M}}$
 613 is one-to-one (isomorphism is supposed to preserve structure, not sure how to
 614 interpret that here). Since we have simulated values of this map on a regular
 615 grid in the detector space \mathcal{D} , we also know the inverse map $\bar{\mathcal{M}}^{-1}$ on the irregular
 616 inverse grid in the readout space \mathcal{R} . To get an approximation of the inverse map
 617 in the entire readout space, we can use interpolation.

618 Since the inverse grid is irregular, trilinear interpolation cannot be applied.
 619 Given that the simulated map is dense enough to provide a good approxima-
 620 tion considering the size of our pads, we can adopt a similar approach (more
 621 complicated and computationally heavy alternative would be natural neighbor
 622 interpolation). As shown in Equation 1.20 in Section 1.3.3, trilinear interpolation
 623 can be expressed as a polynomial:

$$\hat{f}(x, y, z) = axyz + bxy + cxz + dyz + ex + fy + gz + h, \quad (3.14)$$

624 where a, b, c, d, e, f, g, h are coefficients uniquely determined by the values of
 625 the function at the vertices of the interpolation cell. We can generalize this
 626 for a function defined on an irregular grid. Given the function values at any eight
 627 points, we can write a system of eight linear equations

$$\begin{pmatrix} x_1y_1z_1 & x_1y_1 & x_1z_1 & y_1z_1 & x_1 & y_1 & z_1 & 1 \\ \vdots & \vdots \\ x_8y_8z_8 & x_8y_8 & x_8z_8 & y_8z_8 & x_8 & y_8 & z_8 & 1 \end{pmatrix} \begin{pmatrix} a \\ \vdots \\ h \end{pmatrix} = \begin{pmatrix} f(x_1, y_1, z_1) \\ \vdots \\ f(x_8, y_8, z_8) \end{pmatrix}, \quad (3.15)$$

628 which has a unique solution for the coefficients for most values of (x_n, y_n, z_n) and
 629 $f(x_n, y_n, z_n)$, where $n \in \{1, \dots, 8\}$.

630 This approach introduces a small complication: finding the correct pseudocell
 631 (i.e., the image of eight vertices forming a cubic cell in the regular grid) in
 632 the inverse grid. The eight irregularly spaced vertices of this pseudocell do not
 633 define a unique volume, so there are multiple possible ways to partition \mathcal{R} into
 634 pseudocells, with no obvious choice among them.

635 We are currently ignoring this problem and performing binary search along
 636 x, y, z (in this order). It shouldn't matter too much because the 70/30 map

637 doesn't cause such a big distortion and was even accidentally extrapolated for all
 638 z different from the central plane. Interpolation should be generally faster than
 639 the gradient descent since we don't need to iterate. We also don't need to optimize
 640 it to improve performance, if it's too slow we can even calculate the coefficients
 641 for the entire map before reconstruction.

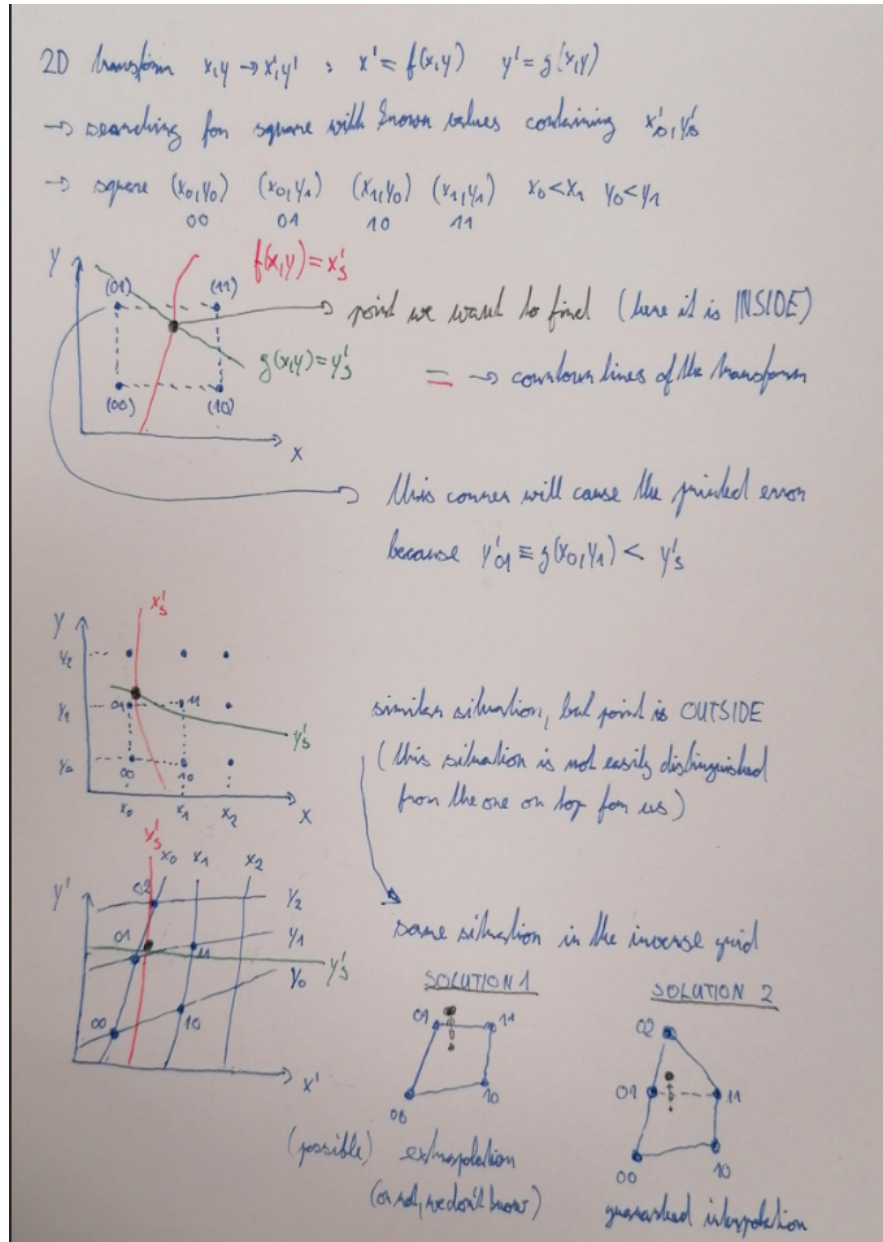


Figure 3.6: Selection of the points for interpolation. Create better images; use the explanation interpolation vs. extrapolation strange property. Solution 2 probably does not make much sense.

642 3.3 Discrete Reconstruction

643 Reconstruction with pads and time bins. Maybe testing different pads. Mapping
 644 the center of the pad (along with the midpoint of the time bin) isn't necessarily

645 the best approach since it might not correspond to the average parameters of
 646 an electron with these readout parameters (insignificant?).

647 It is also possible to make this a subsection of the map, making the previous
 648 subsections parts of a new subsection 'Map Inversion'

649 In order to get a more realistic representation of a track measured in the OFTPC,
 650 we need to take the discretization of the position and time data into account.
 651 The readout of the OFTPC will consist of 128 pads, their layout is shown in
 652 Figure 1.4. Time will be read out with $t_{\text{int}} = 100$ ns intervals.

653 As a first approximation, we can neglect the multiplication in the triple-GEM
 654 and assume an ideal charge readout. The time is started at the beginning of
 655 the electron/positron simulation (randomize this time a bit and see what it does
 656 to the reconstruction). The readout coordinates $(x', y', t) \in \mathcal{R}$ of each ionization
 657 electron can be mapped to the pad coordinates $(n_{\text{pad}}, n_t) \in \mathcal{P}$ (using the param-
 658 eters described in Section 1.3.2):

$$n_{\text{pad}} = n: (x', y') \in \left[x_{1,n} - \frac{g}{2}, x_{2,n} + \frac{g}{2} \right] \times \left[y_{1,n} - \frac{g}{2}, y_{2,n} + \frac{g}{2} \right], \quad (3.16)$$

$$n_t = \left\lceil \frac{t}{t_{\text{int}}} \right\rceil. \quad (3.17)$$

659 This way the closest pad is assigned to each readout position within the OFTPC
 660 volume². Makes sense since the pads attract the electrons, the inhomogeneity of
 661 electric field is neglected. The number of electrons in each pad (i.e., collected
 662 charge) is then counted and serves as a weight for the energy reconstruction.
 663 The reconstructed track consists of points for each $(n, n_t) \in \mathcal{P}$, we get these by
 664 reconstructing the position of a hypothetical electron with the readout coordi-
 665 nates of the pad/time bin center:

$$\mathcal{D} \ni (x, y, z) = \overline{\mathcal{M}} \left(x_{c,n}, y_{c,n}, \left(n_t - \frac{1}{2} \right) t_{\text{int}} \right). \quad (3.18)$$

²Some positions near the wall are not handled and some pads extend beyond the OFTPC volume.

666 4. Energy Reconstruction

667 The second stage is the reconstruction of the particle's energy using a fit of its
668 reconstructed track (see Section 3). We have tested three ways of reconstructing
669 the energy. Fitting is done using the MINUIT algorithm implemented in
670 ROOT [2]. **Cite some CERN article directly on MINUIT, can add a section.**

671 The **Cubic Spline Fit** is a tested and later rejected method of energy re-
672 construction. It uses smoothly connected piecewise cubic polynomials between
673 uniformly spaced nodes. Energy is calculated using the fit parameters by comput-
674 ing the radius of curvature in different points of the fitted curve using the known
675 magnitude of the magnetic field perpendicular to the trajectory. We rejected this
676 method because tuning of the fit to have a reasonably stable radius of curvature
677 turned out to be unpractical.

678 The **Circle and Lines Fit** was chosen as an alternative since this corre-
679 sponds to the shape of a trajectory of a charged particle crossing a finite volume
680 with a homogeneous magnetic field. The energy of the particle can be estimated
681 using the fitted radius and the magnitude of the perpendicular magnetic field in
682 the middle of the TPC.

683 The **Runge-Kutta Fit** uses the 4th order Runge-Kutta numerical integration
684 described in Section 2.2. Initial parameters of the track (including the particle's
685 energy) are optimized so that the integrated trajectory fits to the reconstructed
686 one. This fit can also be performed as a single parameter (i.e., energy) fit if we
687 get the initial position and orientation of the particle on the entrance to the TPC
688 from previous detectors (Tpx3 and MWPC, see Section 0.2).

689 4.1 Cubic Spline Fit

690 The first attempt to get an early estimate of the kinetic energy of the particle
691 uses a cubic spline fit. We use an electron track starting in the origin of our
692 coordinate system with an initial direction in the positive x axis. The example
693 track is simulated microscopically (see Section 2.1) with a kinetic energy of 8 MeV
694 in a gas mixture 90% Ar + 10% CO₂ (the same track was used in Section 3.1).
695 **This track should probably be described in the simulation chapter.**

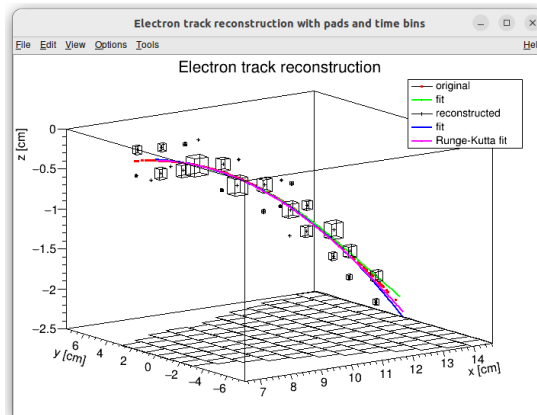


Figure 4.1: Example of a fitted reconstructed track. **Swap for better image.**

696 In order to calculate the spline, we use the class *TSpline3* from ROOT. This
 697 allows us to evaluate the spline using the coordinates (x_n, z_n) of each node and
 698 the derivatives d_1, d_2 in the first and the last node. We can fit these parameters
 699 of a fixed amount of nodes to the simulated trajectory. We use the IMPROVE
 700 algorithm provided by the *TMinuit* class in ROOT. This algorithm attempts to
 701 find a better local minimum after converging.

702 After the fit, we want to get an energy estimate. In order to calculate it, we
 703 need the radius of curvature, which we get from the fitted spline at every point
 704 of the trajectory. The part of the spline corresponding to a given node is defined
 705 as

$$z(x) = z_n + b\Delta x + c(\Delta x)^2 + d(\Delta x)^3, \quad (4.1)$$

706 where $\Delta x = x - x_n$ and b, c, d are coefficients. Using this equation, we derive
 707 the radius of curvature¹ as:

$$r(x) = \frac{(1 + z'^2(x))^{\frac{3}{2}}}{z''(x)} = \frac{(1 + (b + 2c\Delta x + 3d(\Delta x)^2)^2)^{\frac{3}{2}}}{2c + 6d\Delta x}. \quad (4.2)$$

708 Based on the geometry of the detector, we can assume the magnetic field
 709 $\mathbf{B}(x, 0, z) = (0, B(x, z), 0)$ for a track in the XZ plane. Since the electron is rela-
 710 tivistic, the effect of the electric field on its trajectory is negligible. The Lorentz
 711 force \mathbf{F}_L is then always perpendicular to the momentum of the electron and acts
 712 as a centripetal force \mathbf{F}_c :

$$\mathbf{F}_L = \mathbf{F}_c, \quad (4.3)$$

$$\|e\mathbf{v} \times \mathbf{B}\| = \frac{\gamma m_e v^2}{r}, \quad (4.4)$$

$$ec\beta B = \frac{E_{0e}\beta^2}{r\sqrt{1 - \beta^2}}, \quad (4.5)$$

$$\sqrt{1 - \beta^2} = \frac{E_{0e}\beta}{ecBr}, \quad (4.6)$$

713

$$\beta^2(x) = \left[1 + \left(\frac{E_{0e}}{ecB(x, z(x))r(x)} \right)^2 \right]^{-1}, \quad (4.7)$$

714 where e is the elementary charge, c is the speed of light in vacuum, m_e is the rest
 715 mass of electron, $E_{0e} = m_e c^2$ is the corresponding energy, γ is the Lorentz factor,
 716 \mathbf{v} is the velocity of the electron, and $\beta = \frac{v}{c}$. We can then finally get our estimate
 717 of the kinetic energy for a given point on the trajectory as follows:

$$E_{\text{kin}}(x) = \left(\frac{1}{\sqrt{1 - \beta^2(x)}} - 1 \right) E_{0e}. \quad (4.8)$$

718 We can then average these estimates at multiple points to get one final estimate.
 719 This method was later rejected in favor of the circle and lines fit described in
 720 Section 4.2. **Add some figures.**

¹For the general formula see https://en.wikipedia.org/wiki/Curvature#Graph_of_a_function

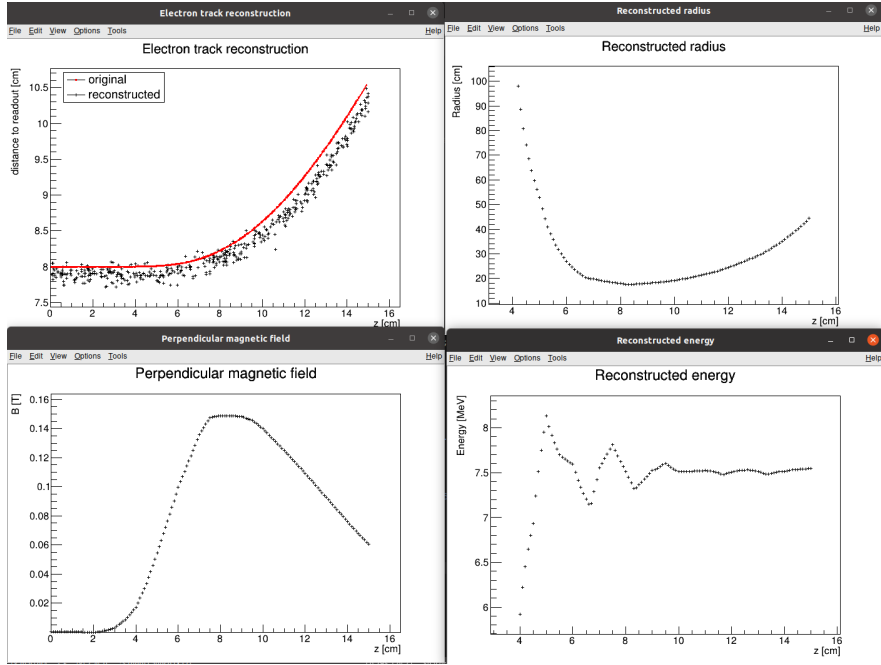


Figure 4.2: First attempt at a track reconstruction using only the drift velocity. Spline energy reconstruction attempt. Swap for better image(s) – subfigure environment, correct coordinates.

721 4.2 Circle and Lines Fit

722 Another way to estimate the particle's kinetic energy is to fit its trajectory with
 723 a circular arc with lines attached smoothly. This shape of trajectory corresponds
 724 to a movement of a charged particle through a homogeneous magnetic field per-
 725 pendicular to the particle's momentum and limited to a certain volume. In gen-
 726 eral, the shape of such a trajectory in a non-perpendicularly oriented field is
 727 a spiral. In our case, this component is negligible since the field is approxi-
 728 mately toroidal and the particle motion is nearly perpendicular to it. At first, we tested
 729 a 2D version of this fit, then we adapted it to 3D.

730 Our field is not homogeneous, it is therefore not entirely clear what value of
 731 magnetic field should be used along with the fitted radius (using equations 4.7
 732 and 4.8) to get the best estimate for the kinetic energy. Since we only use this
 733 method as the first iteration of the particle's energy that we later refine, an op-
 734 timal solution of this problem is not required. Instead, we tested two options:
 735 taking the value of the field in the middle of the fitted circular arc and taking
 736 the average field along it. We haven't really tried to plot this for multiple tracks,
 737 but these estimates are saved somewhere and could be plotted.

738 4.2.1 Two-dimensional fit

739 In the 2D case, the fitted function used for the electron track² described in Sec-
 740 tion 4.1 is defined as follows: Maybe describe this track that we used at the be-
 741 ginning somewhere earlier (section microscopic simulations → Testing track?) so
 742 that it is easier to refer to it in multiple sections. It is not part of the early GitHub

²Electron tracks bend towards negative z , we need to use the upper part of the circle

743 commits, so maybe it won't be possible to create exact replicas of the images,
 744 but they should be at least very similar.

$$z(x) = \begin{cases} a_1x + b_1 & x < x_1 \\ z_0 + \sqrt{r^2 - (x - x_0)^2} & x_1 \leq x \leq x_2, \\ a_2x + b_2 & x > x_2 \end{cases} \quad (4.9)$$

745 where $a_{1,2}$ and $b_{1,2}$ are the parameters of the lines, (x_0, z_0) is the center of the cir-
 746 cle, r is its radius, and $(x_{1,2}, z_{1,2})$ are the coordinates of the function's nodes.
 747 That means we have 9 parameters ($z_{1,2}$ are not used in the function) along with
 748 2 continuity conditions and 2 smoothness conditions. For the fit, we use the co-
 749 ordinates of the nodes and the radius of the circle, which gives us 5 independent
 750 parameters (only the radius has to be larger than half of the distance between
 751 nodes). The continuity conditions (combined with the relations for $z_{1,2}$) are as
 752 follows:

$$z_{1,2} = a_{1,2}x_{1,2} + b_{1,2} = z_0 - \sqrt{r^2 - (x_{1,2} - x_0)^2}. \quad (4.10)$$

753 The smoothness conditions are as follows:

$$a_{1,2} = \frac{x_0 - x_{1,2}}{\sqrt{r^2 - (x_{1,2} - x_0)^2}}. \quad (4.11)$$

754 Equation 4.10 gives us the values of $b_{1,2}$

$$b_{1,2} = z_{1,2} - a_{1,2}x_{1,2}. \quad (4.12)$$

755 For the coordinates of the center of the circle, we can use the fact that the center
 756 has to lie on the axis of its chord. In other words, there is a value of a parameter t
 757 such that, using the parametric equation of the axis

$$\begin{pmatrix} x_0 \\ z_0 \end{pmatrix} = \begin{pmatrix} \frac{x_1+x_2}{2} \\ \frac{z_1+z_2}{2} \end{pmatrix} + t \begin{pmatrix} \frac{z_2-z_1}{2} \\ \frac{x_1-x_2}{2} \end{pmatrix}. \quad (4.13)$$

758 At the same time, the center has to be in a distance of r from the nodes:

$$(x_1 - x_0)^2 + (z_1 - z_0)^2 = r^2, \quad (4.14)$$

$$\left(\frac{x_1 - x_2}{2} + \frac{z_1 - z_2}{2} t \right)^2 + \left(\frac{z_1 - z_2}{2} + \frac{x_2 - x_1}{2} t \right)^2 = r^2, \quad (4.15)$$

$$\left(\left(\frac{x_2 - x_1}{2} \right)^2 + \left(\frac{z_2 - z_1}{2} \right)^2 \right) t^2 + \left(\frac{x_2 - x_1}{2} \right)^2 + \left(\frac{z_2 - z_1}{2} \right)^2 - r^2 = 0. \quad (4.16)$$

759 Since our electron track bends towards negative z and $x_2 > x_1$, we only care
 760 about the solution with $t > 0$

$$t = \sqrt{\frac{r^2}{\left(\frac{x_2 - x_1}{2} \right)^2 + \left(\frac{z_2 - z_1}{2} \right)^2} - 1}, \quad (4.17)$$

761

$$x_0 = \frac{x_1 + x_2}{2} + \frac{z_2 - z_1}{2} \sqrt{\frac{r^2}{\left(\frac{x_2 - x_1}{2} \right)^2 + \left(\frac{z_2 - z_1}{2} \right)^2} - 1}, \quad (4.18)$$

$$z_0 = \frac{z_1 + z_2}{2} - \frac{x_2 - x_1}{2} \sqrt{\frac{r^2}{\left(\frac{x_2 - x_1}{2} \right)^2 + \left(\frac{z_2 - z_1}{2} \right)^2} - 1}. \quad (4.19)$$

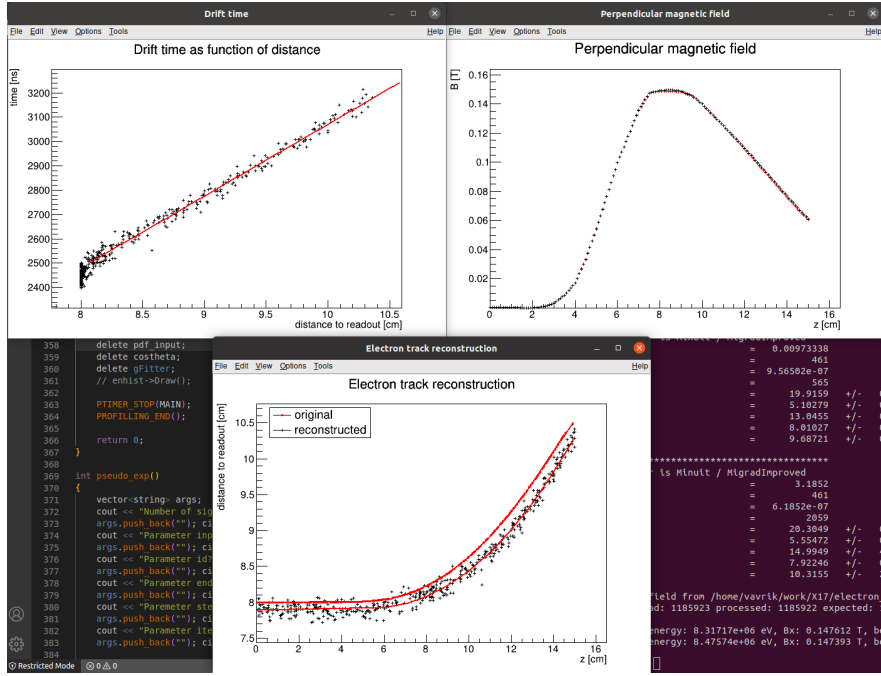


Figure 4.3: First attempt at a track reconstruction using only the drift velocity. Circle and Lines Fit in 2D. Swap for better image, correct coordinates.

762 The function defined in Equation 4.9 along with equations 4.11, 4.12, 4.18 and 4.19
 763 derived using the continuity and smoothness conditions (combined with the re-
 764 lations for $z_{1,2}$) fully define our fitted function with parameters $r, x_{1,2}, z_{1,2}$. Some
 765 pictures of the fit on the tested track. Results of the fit. Again, the actual fit
 766 uses 8-z. Use GeoGebra schematics to generate a picture of 2D geometry.

767 4.2.2 Three-dimensional fit

768 Explain the geometry and least square method used for the 3D fit. Tested on
 769 a Runge-Kutta sample, and with microscopic tracks + map simulation.

770 In three dimensions, the shape of a trajectory of a charged particle in a uniform
 771 magnetic field is a cylindrical helix. since we assume that the field is approxi-
 772 mately perpendicular to the particle's momentum at all times, we will further
 773 approximate the trajectory with a circular arc (with lines attached smoothly).

774 We assume that the initial position $\mathbf{X}_0 = (x_0, y_0, z_0)$ and direction θ, φ (spher-
 775 ical angles as in Section 1.3.2) are known, since this information will be provided
 776 by Tpx3 and MWPC layers. We could further refine it at the end of the current
 777 algorithm with some kind of global fit (all detector layers). The fit then has four
 778 free parameters (figure):

- 779 • the length of the first line l (as measured from the initial position),
- 780 • the radius of the circular arc r ,
- 781 • the central angle of the arc $\phi_{\max} \in [0, 2\pi]$,
- 782 • the direction of the curvature given by the angle $\alpha \in [0, 2\pi]$ (right-handed
 783 with respect to the particle direction, $\alpha = 0$ if the particle curves towards
 784 negative z in a plane given by \hat{z} and the direction vector).

785 Using these parameters, we can derive a parametrization of the whole curve. Let

786 \mathbf{v} be the initial unit direction vector, i.e., using the spherical angles

$$\mathbf{v} = (\cos \varphi \cos \theta, \sin \varphi \cos \theta, \sin \theta)^T, \quad (4.20)$$

787 then we can parameterize the first line as follows:

$$\mathbf{X}_{L1}(t) = \mathbf{X}_0 + t\mathbf{v} \quad t \in [0, l]. \quad (4.21)$$

788 This gives us the starting point of the arc

$$\mathbf{X}_1 = \mathbf{X}_{L1}(l) = \mathbf{X}_0 + l\mathbf{v}. \quad (4.22)$$

789 The vector $\mathbf{n} \perp \mathbf{c}_1$ that lies in the plane of curvature and points from \mathbf{X}_1 to
790 the center of curvature can be calculated using a composition of rotations. First,
791 we rotate \mathbf{v} to point in the $\hat{\mathbf{x}}$ direction, the normal for $\alpha = 0$ than points in
792 the $-\hat{\mathbf{z}}$ direction, we apply the α rotation and reverse the rotations into the $\hat{\mathbf{x}}$
793 direction:

$$\begin{aligned} \mathbf{c}_1 &= R_z(\varphi)R_y(-\theta)R_x(\alpha)R_y\left(\frac{\pi}{2}\right)R_y(\theta)R_z(-\varphi)\mathbf{v}, \\ &= R_z(\varphi)R_y(-\theta)R_x(\alpha)(-\hat{\mathbf{z}}), \\ &= \begin{pmatrix} \cos \varphi & -\sin \varphi & 0 \\ \sin \varphi & \cos \varphi & 0 \\ 0 & 0 & 1 \end{pmatrix} \begin{pmatrix} \cos \theta & 0 & -\sin \theta \\ 0 & 1 & 0 \\ \sin \theta & 0 & \cos \theta \end{pmatrix} \begin{pmatrix} 1 & 0 & 0 \\ 0 & \cos \alpha & -\sin \alpha \\ 0 & \sin \alpha & \cos \alpha \end{pmatrix} \begin{pmatrix} 0 \\ 0 \\ -1 \end{pmatrix}, \quad (4.23) \\ &= \begin{pmatrix} -\sin \alpha \sin \varphi + \cos \alpha \cos \varphi \sin \theta \\ \sin \alpha \cos \varphi + \cos \alpha \sin \varphi \sin \theta \\ -\cos \alpha \cos \theta \end{pmatrix}. \end{aligned}$$

794 Seems like in this part of the code θ is actually taken from the pole. Similarly by
795 rotating $\hat{\mathbf{y}}$, we can get the normal vector $\mathbf{n} = \mathbf{v} \times \mathbf{c}_1$ perpendicular to the plane
796 of the trajectory:

$$\mathbf{n} = R_z(\varphi)R_y(-\theta)R_x(\alpha)\hat{\mathbf{y}} = \begin{pmatrix} -\cos \alpha \sin \varphi - \sin \alpha \cos \varphi \sin \theta \\ \cos \alpha \cos \varphi - \sin \alpha \sin \varphi \sin \theta \\ \sin \alpha \cos \theta \end{pmatrix}. \quad (4.24)$$

797 This allows us to express the coordinates of the center of the circular arc:

$$\mathbf{C} = \mathbf{X}_1 + r\mathbf{c}_1. \quad (4.25)$$

798 We can then get the parametrization and the endpoint of the circular arc using
799 Rodrigues' rotation formula:

$$\begin{aligned} \mathbf{c}_2 &= \mathbf{c}_1 \cos \phi_{\max} + (\mathbf{n} \times \mathbf{c}_1) \sin \phi_{\max} + \mathbf{n}(\mathbf{n} \cdot \mathbf{c}_1)(1 - \cos \phi_{\max}), \\ &= \mathbf{c}_1 \cos \phi_{\max} - \mathbf{v} \sin \phi_{\max}, \end{aligned} \quad (4.26)$$

$$\mathbf{X}_C(\phi) = \mathbf{C} - r(\mathbf{c}_1 \cos \phi - \mathbf{v} \sin \phi) \quad \phi \in [0, \phi_{\max}], \quad (4.27)$$

$$\mathbf{X}_2 = \mathbf{X}_C(\phi_{\max}) = \mathbf{C} - r\mathbf{c}_2, \quad (4.28)$$

800 and if we define the direction vector of the second line, we also get its parametriza-
801 tion

$$\mathbf{w} = \mathbf{v} \cos \phi_{\max} + (\mathbf{n} \times \mathbf{v}) \sin \phi_{\max} = \mathbf{v} \cos \phi_{\max} + \mathbf{c}_1 \sin \phi_{\max}, \quad (4.29)$$

$$\mathbf{X}_{L2}(s) = \mathbf{X}_2 + s\mathbf{w} \quad s \in [0, \infty). \quad (4.30)$$

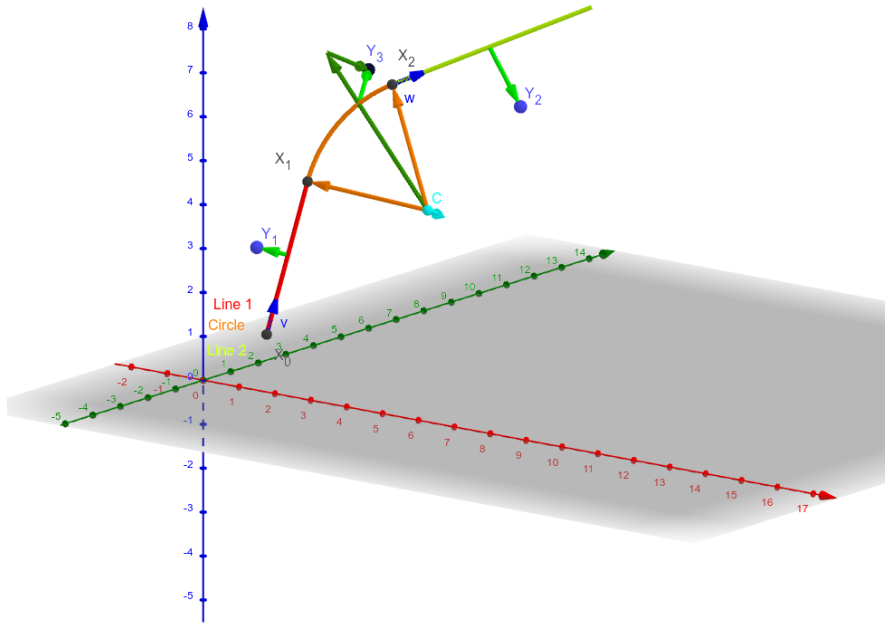


Figure 4.4: Circle and Lines Fit 3D geometry. Swap for better image.

802 The fit is performed as a (weighted) least square minimization (**MIGRAD**
 803 **ROOT**), therefore we need to derive the distance of any point \mathbf{P} to the fitted
 804 curve. For the first line, we simply compute the parameter value of the closest
 805 point on the line:

$$t_P = \mathbf{v} \cdot (\mathbf{P} - \mathbf{X}_1), \quad (4.31)$$

$$d_{P1} = \|\mathbf{P} - \mathbf{X}_{L1}(t_P)\|. \quad (4.32)$$

806 If the parameter value is outside of its bounds defined above, we take the bound-
 807 ary value instead. The distance to the second line is computed likewise. For
 808 the circular arc, we find the closest point by projecting the center connecting line
 809 onto the arc plane:

$$\mathbf{X}_{PC} = \mathbf{X}_C + r \frac{(\mathbf{P} - \mathbf{X}_C) - (\mathbf{n} \cdot (\mathbf{P} - \mathbf{X}_C))\mathbf{n}}{\|(\mathbf{P} - \mathbf{X}_C) - (\mathbf{n} \cdot (\mathbf{P} - \mathbf{X}_C))\mathbf{n}\|}, \quad (4.33)$$

$$d_{PC} = \|\mathbf{P} - \mathbf{X}_{PC}\| \quad (4.34)$$

810 Potential problem in the implementation – might not be correctly handling ϕ
 811 out of bounds, the distance could be sometimes underestimated because of this.
 812 The shortest distance out of d_{P1}, d_{PC}, d_{P2} is then taken as the distance to the curve.
 813 When calculating energy with the average field, only the arc is considered. Mid-
 814 dle field in the current implementation taken in the middle x plane (intersection
 815 with the curve). TVirtualFitter+MIGRAD.

816 4.3 Runge-Kutta Fit

817 Single parameter fit with 4th order Runge-Kutta simulated track. Future testing
 818 with microscopic simulations and map simulation. Derivation of the geometry

819 (least squares).

Conclusion

821 Here or at the end of each section. Something about the future of this work?

822 Notes

823 General notes about the thesis:

- 824 • Check that all of the classes and other code are marked the same way in
825 the text. I used italics somewhere, could use different font for this instead.
- 826 • Check unbreakable space in front of articles. Remove excessive article usage
827 with proper nouns.
- 828 • Currently using margins for single-sided printing (bigger on the left side).
- 829 • Check that present tense is used
- 830 • Active vs passive voice usage
- 831 • American English quotation marks (") instead of British English (').
- 832 • Some of the overfull hbox warnings might change if duplex printing is used
833 (they generate black rectangles on the edge of the page), leaving them be
834 for now
- 835 • Check nobreakdash usage (is it always necessary)
- 836 • Check capitalized references (e.g., Figure, Section, Equation)
- 837 • Check $\backslash(...\backslash)$ math mode instead of $\$...$$. (actually unlike $\backslash[...\backslash]$ math mode,
838 there is apparently no real benefit to this clumsy syntax)
- 839 • Use siunitx package to ensure correct formatting.
- 840 • Check other stuff that's written in the MFF UK template. Apparently it
841 has since been updated and there are some differences (check for them).
- 842 • Check correct subscripts in equation (italics vs no italics)
- 843 • Consistent bold marking of points/vectors
- 844 • Correct footnotes (capital letters, etc.).

845 Random notes:

- 846 • Terminology consistency – ionization/primary/secondary electrons
- 847 • Consistent TPC vs OFTPC acronym usage in the text or individual chap-
848 ters.
- 849 • Only electrons that start and end in the sector closer than 0.5 cm are used
850 for reconstruction (newest version).
- 851 • Attachment, Penning transfer and secondary ionization not considered in
852 the microscopic simulation.

- 853 • Suspicious artifacts of trilinear interpolation in Figure 1.5. **Fixed – integers instead of doubles in the implementation, influenced reconstruction SIGNIFICANTLY (but not simulation).**
- 854
- 855

856

Future

857 Things planned for the future:

- 858 • Testing the reconstruction algorithm by measuring real particles with a known energy distribution.
- 859
- 860 • The **Fast Simulation with Ionization Electron Map** is planned for the future. It will use the HEED program [27] to simulate the primary particle and the Ionization Electron Map (see Section 3.2) to simulate the drift of secondary electrons. It should be significantly faster than the Microscopic Simulation but offer comparable precision since it will rely on an already simulated drift map. (Primary track simulated in HEED. Readout parameters by interpolating the map. Diffusion from the map for randomization.)
- 861
- 862
- 863
- 864
- 865
- 866
- 867
- 868
- 869
- 870
- 871
- 872
- 873
- 874
- 875
- 876
- 877
- 878
- 879
- 880
- 881
- 882
- 883
- 884
- 885
- 886
- 887
- 888
- 889
- 890
- Account for GEM, delta electrons, ...
 - Likelihood approach instead of least squares (if it improves the reconstruction significantly), we should at least use a better method than taking the center of the TPC bin.
 - More detailed electric field simulation (if needed, GEM will have more complex field)

Likelihood - inverse map

If we wanted to further improve this procedure, taking into account the whole map \mathcal{M} , we could make an "inverse map" from \mathcal{R} to distributions on \mathcal{D} . We could achieve this by taking the normalized probability density of an electron with initial coordinates (x, y, z) having readout coordinates (x', y', t) . If we fix (x', y', t) , we get an unnormalized probability density $f(x, y, z) = \mathcal{M}_{(x,y,z)}(x', y', t)$ (assuming that all initial coordinates are a priori equally likely). This could potentially improve the discrete reconstruction if we take the mean value of this probability density across the pad and time bin

$$f_{\text{pad, bin}}(x, y, z) = \frac{1}{A_{\text{pad}} \Delta t_{\text{bin}}} \int_{\text{pad, bin}} \mathcal{M}_{(x,y,z)}(x', y', t) dx' dy' dt \quad (4.35)$$

and using it for a likelihood fit instead of using least squares. This still assumes that all initial coordinates are equally likely which is clearly not the case for a primary particle track. In the future, we could even use the fast track simulation with the map (should be possible to make around 1000 tracks per minute per core with current settings), create a big set of tracks with reasonable parameters and use these to get an approximation of the probability distribution of the detector response. Some approximations would be necessary when interpreting the data to decrease the degrees of freedom of this distribution (we would have to pick a set of parameters and assume that some of them are independent). This could give us

891 an idea about the best achievable resolution (how significantly will the detector
892 response differ for a given change in energy). If the difference is significant, we
893 could try to further improve the likelihood fit.

Bibliography

- [1] Garfield++. <https://garfieldpp.web.cern.ch/garfieldpp/>. Accessed: 2023-05-18.
- [2] Rene Brun and Fons Rademakers. Root — An Object Oriented Data Analysis Framework. *Nuclear Instruments and Methods in Physics Research Section A: Accelerators, Spectrometers, Detectors and Associated Equipment*, 389(1–2):81–86, Apr 1997. Proceedings AIHENP’96 Workshop, Lausanne, Sep. 1996, See also <https://root.cern/>, Paper published in the Linux Journal, Issue 51, July 1998.
- [3] About MetaCentrum. <https://metavo.metacentrum.cz/en/about/index.html>, 2023. Accessed: 2024-11-27.
- [4] M. E. Rose. Internal Pair Formation. *Phys. Rev.*, 76:678–681, Sep 1949.
- [5] R. Essig, J. A. Jaros, W. Wester, P. Hansson Adrian, S. Andreas, T. Averett, O. Baker, B. Batell, M. Battaglieri, J. Beacham, T. Beranek, J. D. Bjorken, F. Bossi, J. R. Boyce, G. D. Cates, A. Celentano, A. S. Chou, R. Cowan, F. Curciarello, H. Davoudiasl, P. deNiverville, R. De Vita, A. Denig, R. Dharmapalan, B. Dongwi, B. Döbrich, B. Echenard, D. Espriu, S. Fegan, P. Fisher, G. B. Franklin, A. Gasparian, Y. Gershtein, M. Graham, P. W. Graham, A. Haas, A. Hatzikoutelis, M. Holtrop, I. Irastorza, E. Izaguirre, J. Jaeckel, Y. Kahn, N. Kalantarians, M. Kohl, G. Krnjaic, V. Kubarovský, H-S. Lee, A. Lindner, A. Lobanov, W. J. Marciano, D. J. E. Marsh, T. Maruyama, D. McKeen, H. Merkel, K. Moffeit, P. Monaghan, G. Mueller, T. K. Nelson, G. R. Neil, M. Oriunno, Z. Pavlovic, S. K. Phillips, M. J. Pivovaroff, R. Poltis, M. Pospelov, S. Rajendran, J. Redondo, A. Ringwald, A. Ritz, J. Ruz, K. Saenboonruang, P. Schuster, M. Shinn, T. R. Slatyer, J. H. Steffen, S. Stepanyan, D. B. Tanner, J. Thaler, M. E. Tobar, N. Toro, A. Upadye, R. Van de Water, B. Vlahovic, J. K. Vogel, D. Walker, A. Weltman, B. Wojtsekhowski, S. Zhang, and K. Zioutas. Dark Sectors and New, Light, Weakly-Coupled Particles, 2013.
- [6] F.W.N. de Boer, O. Fröhlich, K.E. Stiebing, K. Bethge, H. Bokemeyer, A. Balandia, A. Buda, R. van Dantzig, Th.W. Elze, H. Folger, J. van Klinken, K.A. Müller, K. Stelzer, P. Thee, and M. Waldschmidt. A deviation in internal pair conversion. *Physics Letters B*, 388(2):235–240, 1996.
- [7] F W N de Boer, R van Dantzig, J van Klinken, K Bethge, H Bokemeyer, A Buda, K A Müller, and K E Stiebing. Excess in nuclear pairs near 9 MeV/ invariant mass. *Journal of Physics G: Nuclear and Particle Physics*, 23(11):L85, nov 1997.
- [8] F W N de Boer, K Bethge, H Bokemeyer, R van Dantzig, J van Klinken, V Mironov, K A Müller, and K E Stiebing. Further search for a neutral boson with a mass around 9 MeV/c². *Journal of Physics G: Nuclear and Particle Physics*, 27(4):L29, apr 2001.

- 935 [9] Attila Vitéz, A. Krasznahorkay, J. Gulyas, Margit Csatlos, Lorant Csige,
 936 Zoltan Gacsi, Barna Nyakó, F. Boer, T. Ketel, and J. Klinken. Anomalous
 937 Internal Pair Creation in ${}^8\text{Be}$ as a Signature of the Decay of a New Particle.
 938 *Acta Physica Polonica B - ACTA PHYS POL B*, 39:483, 02 2008.
- 939 [10] A. Krasznahorkay, J. Gulyas, Margit Csatlos, Attila Vitéz, T. Tornyi,
 940 L. Stuhl, Lorant Csige, Zoltan Gacsi, A. J. Krasznahorkay, M. Hunyadi,
 941 and T.J. Ketel. Searching for a light neutral axial-vector boson in isoscalar
 942 nuclear transitions. *Frascati Physics Series*, 56:86, 10 2012.
- 943 [11] A. J. Krasznahorkay, M. Csatlós, L. Csige, Z. Gácsi, J. Gulyás, M. Hunyadi,
 944 I. Kuti, B. M. Nyakó, L. Stuhl, J. Timár, T. G. Tornyi, Zs. Vajta, T. J. Ketel,
 945 and A. Krasznahorkay. Observation of Anomalous Internal Pair Creation
 946 in ${}^8\text{Be}$: A Possible Indication of a Light, Neutral Boson. *Physical Review
 947 Letters*, 116(4), January 2016.
- 948 [12] D.R. Tilley, J.H. Kelley, J.L. Godwin, D.J. Millener, J.E. Purcell, C.G. Sheu,
 949 and H.R. Weller. Energy levels of light nuclei $A=8,9,10$. *Nuclear Physics A*,
 950 745(3):155–362, 2004.
- 951 [13] N. J. Sas, A. J. Krasznahorkay, M. Csatlós, J. Gulyás, B. Kertész, A. Krasznahorkay,
 952 J. Molnár, I. Rajta, J. Timár, I. Vajda, and M. N. Harakeh. Observation of the X17 anomaly in the ${}^7\text{Li}(p,e^+e^-){}^8\text{Be}$ direct proton-capture
 953 reaction, 2022.
- 955 [14] A. J. Krasznahorkay, M. Csatlós, L. Csige, J. Gulyás, A. Krasznahorkay,
 956 B. M. Nyakó, I. Rajta, J. Timár, I. Vajda, and N. J. Sas. New anomaly
 957 observed in ${}^4\text{He}$ supports the existence of the hypothetical X17 particle.
 958 *Physical Review C*, 104(4), October 2021.
- 959 [15] D.R. Tilley, H.R. Weller, and G.M. Hale. Energy levels of light nuclei $A =$
 960 4. *Nuclear Physics A*, 541(1):1–104, 1992.
- 961 [16] A. J. Krasznahorkay, A. Krasznahorkay, M. Begala, M. Csatlós, L. Csige,
 962 J. Gulyás, A. Krakó, J. Timár, I. Rajta, I. Vajda, and N. J. Sas. New
 963 anomaly observed in ${}^{12}\text{C}$ supports the existence and the vector character of
 964 the hypothetical X17 boson. *Phys. Rev. C*, 106:L061601, Dec 2022.
- 965 [17] F. Ajzenberg-Selove. Energy levels of light nuclei $A = 11,12$. *Nuclear Physics
 966 A*, 506(1):1–158, 1990.
- 967 [18] Péter Kálmán and Tamás Keszthelyi. Anomalous internal pair creation. *The
 968 European Physical Journal A*, 56, 08 2020.
- 969 [19] A. Aleksejevs, S. Barkanova, Yu. G. Kolomensky, and B. Sheff. A Standard
 970 Model Explanation for the "ATOMKI Anomaly", 2021.
- 971 [20] Jonathan L. Feng, Bartosz Fornal, Iftah Galon, Susan Gardner, Jordan
 972 Smolinsky, Tim M. P. Tait, and Philip Tanedo. Protophobic Fifth-Force
 973 Interpretation of the Observed Anomaly in ${}^8\text{Be}$ Nuclear Transitions. *Phys.
 974 Rev. Lett.*, 117:071803, Aug 2016.

- [21] Tran The Anh, Tran Dinh Trong, Attila J. Krasznahorkay, Attila Krasznahorkay, József Molnár, Zoltán Pintye, Nguyen Ai Viet, Nguyen The Nghia, Do Thi Khanh Linh, Bui Thi Hoa, Le Xuan Chung, and Nguyen Tuan Anh. Checking the ${}^8\text{Be}$ Anomaly with a Two-Arm Electron Positron Pair Spectrometer. *Universe*, 10(4):168, April 2024.
- [22] Kh. U. Abraamyan, Ch. Austin, M. I. Baznat, K. K. Gudima, M. A. Kozhin, S. G. Reznikov, and A. S. Sorin. Observation of structures at ~ 17 and ~ 38 MeV/c^2 in the $\gamma\gamma$ invariant mass spectra in pC, dC, and dCu collisions at p_{lab} of a few GeV/c per nucleon, 2023.
- [23] The MEG II collaboration, K. Afanaciev, A. M. Baldini, S. Ban, H. Benmansour, G. Boca, P. W. Cattaneo, G. Cavoto, F. Cei, M. Chiappini, A. Corvaglia, G. Dal Maso, A. De Bari, M. De Gerone, L. Ferrari Barusso, M. Francesconi, L. Galli, G. Gallucci, F. Gatti, L. Gerritzen, F. Grancagnolo, E. G. Grandoni, M. Grassi, D. N. Grigoriev, M. Hildebrandt, F. Ignatov, F. Ikeda, T. Iwamoto, S. Karpov, P. R. Kettle, N. Khomutov, A. Kolesnikov, N. Kravchuk, V. Krylov, N. Kuchinskiy, F. Leonetti, W. Li, V. Malyshev, A. Matsushita, M. Meucci, S. Mihara, W. Molzon, T. Mori, D. Nicolò, H. Nishiguchi, A. Ochi, W. Ootani, A. Oya, D. Palo, M. Panareo, A. Papa, V. Pettinacci, A. Popov, F. Renga, S. Ritt, M. Rossella, A. Rozhdestvensky, S. Scarpellini, P. Schwendimann, G. Signorelli, M. Takahashi, Y. Uchiyama, A. Venturini, B. Vitali, C. Voena, K. Yamamoto, R. Yokota, and T. Yonemoto. Search for the X17 particle in ${}^7\text{Li}(p, e^+e^-){}^8\text{Be}$ processes with the MEG II detector, 2024.
- [24] Stewart C. Loken, H. Aihara, M. Alston-Garnjost, D. H. Badtke, J. A. Bakken, A. Barbaro-Galtieri, A. V. Barnes, B. A. Barnett, B. Blumenfeld, A. Bross, C. D. Buchanan, W. C. Carithers, O. Chamberlain, J. Chiba, C-Y. Chien, A. R. Clark, O. I. Dahl, C. T. Day, P. Delpierre, K. A. Derby, P. H. Eberhard, D. L. Fancher, H. Fujii, T. Fujii, B. Gabioud, J. W. Gary, W. Gorn, N. J. Hadley, J. M. Hauptman, B. Heck, H. Hilke, J. E. Huth, J. Hylen, H. Iwasaki, T. Kamae, R. W. Kenney, L. T. Kerth, R. Koda, R. R. Kofler, K. K. Kwong, J. G. Layter, C. S. Lindsey, S. C. Loken, X-Q. Lu, G. R. Lynch, L. Madansky, R. J. Madaras, R. Majka, J. Mallet, P. S. Martin, K. Maruyama, J. N. Marx, J. A. J. Matthews, S. O. Melnikoff, W. Moses, P. Nemethy, D. R. Nygren, P. J. Oddone, D. Park, A. Pevsner, M. Pripstein, P. R. Robrish, M. T. Ronan, R. R. Ross, F. R. Rouse, G. Shapiro, M. D. Shapiro, B. C. Shen, W. E. Slater, M. L. Stevenson, D. H. Stork, H. K. Ticho, N. Toge, M. Urban, G. J. Van Dalen, R. van Tyen, H. Videau, M. Wayne, W. A. Wenzel, R. F. vanDaalen Wetters, M. Yamauchi, M. E. Zeller, and W-M. Zhang. Performance of the signal processing system for the time projection chamber. *IEEE Transactions on Nuclear Science*, 30(1):162–166, 1983.
- [25] Misbah Uddin Ahmed. Simulation of the electron and ion movement through a 4-GEM stack, 2021. Institut für Kernphysik.
- [26] Cmglee. Trilinear interpolation visualisation, 2025. Licensed under

1019 CC BY-SA 3.0 ([https://creativecommons.org/licenses/by-sa/3.0/
1020 legalcode](https://creativecommons.org/licenses/by-sa/3.0/legalcode)). Accessed: 26-March-2025.

1021 [27] I.B. Smirnov. Modeling of ionization produced by fast charged particles in
1022 gases. *Nuclear Instruments and Methods in Physics Research Section A: Ac-
1023 celerators, Spectrometers, Detectors and Associated Equipment*, 554(1):474–
1024 493, 2005.

1025 **Acknowledgments:** Computational resources were provided by the e-INFRA
1026 CZ project (ID:90254), supported by the Ministry of Education, Youth and Sports
1027 of the Czech Republic.

1028 List of Figures

1029 0.1	The ATOMKI anomalous IPC measured for different nuclei.	4
1030 0.2	Results from the Hanoi spectrometer – angular e^+e^- pair correlations measured in the ${}^7\text{Li}(p, e^+e^-){}^8\text{Be}$ reaction at $E_p = 1225$ keV [21].	5
1031 0.3	Results from the MEG II experiments – angular correlation of e^+e^- pairs with $E_{\text{sum}} \in [16, 20]$ MeV measured in the ${}^7\text{Li}(p, e^+e^-){}^8\text{Be}$ reaction with proton beam energies 500 and 1080 keV. The 500 keV dataset is fitted with Monte Carlo of both the IPC deexcitation and the EPC produced by gammas [23].	6
1032 0.4	Schematics of the detector at the Van der Graaff facility at IEAP CTU.	6
1033		
1034		
1035		
1036		
1037		
1038 1.1	Schematic view of the PEP-4 TPC [24].	9
1039 1.2	Garfield simulation of an avalanche in a GEM hole [25].	11
1040 1.3	Schematics of the first sector OFTPC with detector space coordinates.	13
1041		
1042 1.5	Magnetic field simulation results. The OFTPC volume and the vacuum tube are marked with black lines, the magnets are marked with red lines. The coordinates of the magnets from the CAD drawing seem to be 9/10 of the ones from the magnetic simulation (confirm and fix).	14
1043		
1044		
1045		
1046		
1047 1.4	Pad layout of the OFTPC and its parameters. Pads 102, 124 and 127 are irregular, the rest has the same dimensions.	14
1048		
1049 1.6	Visualization of trilinear interpolation as a composition of linear interpolations. Image drawn in GeoGebra and inspired by a similar image on Wikipedia (which looks a bit worse) – is credit necessary?	15
1050		
1051		
1052 1.7	Geometric interpretation of trilinear interpolation. The colored dots represent the values in given points and the colored boxes represent the volume by which the corresponding values are multiplied. The black dot represents the interpolated value which is multiplied by the entire volume [26].	16
1053		
1054		
1055		
1056		
1057 2.1	Example of a simulated electron track in 70 % argon and 30 % CO ₂ atmosphere (on the left). Swap for better images, better zoom. Explain drift lines, primary particle.	18
1058		
1059		
1060 2.2	Comparison of diffusion in a simulated electron track in 70 % argon, 30 % CO ₂ atmosphere and in 90 % argon, 10 % CO ₂ atmosphere (on the right). Swap for better image, better zoom. Or put the same pictures for both comparisons in one subfigure, etc. Describe better.	18
1061		
1062		
1063		
1064		
1065 3.1	Dependence of the drift time on the z coordinate in 90 % argon and 10 % CO ₂ atmosphere, fitted with a linear function. The fitted function gives us the average drift velocity in the gas and can be used for rough reconstruction in our TPC. Swap for better image with axis labels, etc. Maybe write the fitted equation.	20
1066		
1067		
1068		
1069		

1070	3.2 First attempt at a track reconstruction using only the drift velocity.	21
1071	This approach works well in a standard TPC (ideally cite some source?). 90 % argon and 10 % CO ₂ atmosphere. Swap for better image, correct coordinates .	
1072		
1073		
1074	3.3 First attempt at a track reconstruction using only the drift velocity, residues. Swap for better image, correct coordinates . What's causing the shift? Explain details.	21
1075		
1076		
1077	3.4 Example of map generation. Swap for better image, correct coordinates .	23
1078		
1079	3.5 Example reconstruction with the map. Swap for better image, correct coordinates .	24
1080		
1081	3.6 Selection of the points for interpolation. Create better images; use the explanation interpolation vs. extrapolation strange property . Solution 2 probably does not make much sense.	26
1082		
1083		
1084	4.1 Example of a fitted reconstructed track. Swap for better image .	28
1085	4.2 First attempt at a track reconstruction using only the drift velocity. Spline energy reconstruction attempt. Swap for better image(s) – subfigure environment, correct coordinates .	30
1086		
1087		
1088	4.3 First attempt at a track reconstruction using only the drift velocity. Circle and Lines Fit in 2D. Swap for better image, correct coordinates .	32
1089		
1090		
1091	4.4 Circle and Lines Fit 3D geometry. Swap for better image .	34

₁₀₉₂ **List of Tables**

¹⁰⁹³ List of Abbreviations

- ¹⁰⁹⁴ **GEM** Gas Electron Multiplier
- ¹⁰⁹⁵ **HEED** High Energy Electro-Dynamics
- ¹⁰⁹⁶ **IEAP CTU** Institute of Experimental and Applied Physics, Czech Technical
¹⁰⁹⁷ University in Prague
- ¹⁰⁹⁸ **IPC** Internal Pair Creation
- ¹⁰⁹⁹ **EPC** External Pair Creation
- ¹¹⁰⁰ **Micromegas** MICRO-MEsh GAseous Structure
- ¹¹⁰¹ **MWPC** Multi-Wire Proportional Chamber
- ¹¹⁰² **OFTPC** Orthogonal Fields TPC
- ¹¹⁰³ **TPC** Time Projection Chamber
- ¹¹⁰⁴ **ToA** time-of-arrival
- ¹¹⁰⁵ **ToT** time-over-threshold
- ¹¹⁰⁶ **Tpx3** Timepix 3